# Non-Hermitian chiral skin effect

Xin-Ran Ma,[1,*] Kui Cao,[1,*] Xiao-Ran Wang,[2] Zheng Wei,[1] Qian Du,[1] and Su-Peng Kou[1,†]
[1]*Center for Advanced Quantum Studies, Department of Physics, Beijing Normal University, Beijing 100875, China*
[2]*College of Teacher Education, Hebei Normal University, Shijiazhuang 050024, China*

(Received 17 June 2023; revised 3 November 2023; accepted 10 January 2024; published 28 February 2024)

The interplay between non-Hermitian effects and topological insulators has become a frontier of research in non-Hermitian physics. However, the existence of a non-Hermitian skin effect for topological-protected edge states remains controversial. In this paper, we discover a new type of the non-Hermitian skin effect called the non-Hermitian chiral skin effect. Non-Hermitian chiral skin effect is induced by inhomogeneous edge dissipation under closed boundary conditions. In particular, the chiral modes of the non-Hermitian chiral skin effect localize around "topological defects" characterized by global dissipation rather than being confined to the system boundaries. We show its detailed physical properties by taking the non-Hermitian Haldane model as an example. As a result, the intrinsic mechanism of the hybrid skin-topological effect in Chern insulators is fully understood via the non-Hermitian chiral skin effect. Therefore this work will be helpful for the research on both non-Hermitian physics and topological quantum states.

DOI: 10.1103/PhysRevResearch.6.013213

## I. INTRODUCTION

The non-Hermitian quantum systems have attracted intensive attention due to their effectiveness in describing nonequilibrium and open systems, as well as their rich underlying physics distinguishing them from Hermitian counterparts [1–8]. There are many intriguing phenomena in non-Hermitian quantum systems, such as exceptional degeneracies [9–11], unidirectional transmission [12,13], and non-Hermitian skin effect [2,14–38]. Non-Hermitian skin effect is widely observed in non-Hermitian systems, highlighting the sensitivity of these systems to the boundary conditions. This sensitivity leads to the difference of wave functions and spectra under periodic boundary conditions (PBC) and open boundary conditions (OBC). To be more precise, the open boundary spectra may collapse compared to the periodic boundary spectra, along with the emergence of non-Hermitian skin modes [39,40].

The studies of the interplay between the non-Hermitian skin effect and topological insulators have uncovered many novel physical phenomena [31]. Over the past five years, the interaction between one-dimensional (1D) boundary states and the non-Hermitian skin effect has been widely studied [18–21,39–49]. However, in recent years, non-Hermitian skin effect in two-dimensional (2D) topological systems has brought about various new effects, such as non-Hermitian Chern bands [50–55], defect-induced non-Hermitian skin effect [56–58], geometry-dependent-skin effect [59,60], and hybrid skin-topological effect [61–64]. The hybrid skin-topological effect is a type of second-order non-Hermitian skin effect of topological edge states that are more accessible to experiments. Recently, considerable progress has been made on the gain/loss induced non-Hermitian skin effect of topological edge states in 2D Chern insulators [63–69]. Initial studies have focused on the staggered gain/loss Haldane model [63,64]. Subsequent research has further expanded our knowledge, revealing that even when sublattice symmetry is disrupted by dissipation, the skin effects of topological edge states can also be observed [67–69]. In such cases, the symmetry of dissipation often imposes specific constraints, causing the skin behavior to rely on the geometry of the open boundary. However, the exact mechanism for topological skin hybridization in different systems is not unified, and there are contradictions in different interpretations.

In our study, we will propose a new mechanism for topological skin hybridization in different systems. To reveal the mechanism of topological skin hybridization, we are naturally led to the following questions: (i) Is the non-Hermitian skin effect that appears in topological edge states of a Chern insulator a new type of non-Hermitian skin effect? How does it relate to the 1D traditional non-Hermitian skin effect? (ii) How can one determine the occurrence of non-Hermitian skin effect in topological edge states, and how can it be characterized? (iii) How do we systematically understand the non-Hermitian skin effect that appears in topological edge states under different types of dissipation in 2D Chern insulators? After answering all the above three questions, we found that the key point is the so-called non-Hermitian chiral skin effect, of which topological edge states in a novel system are predicted to be localized around domain walls of dissipation.

This work is organized as follows. In Sec. II, we provide the analysis of boundary conditions of topological edge states, which is essential for understanding the non-Hermitian chiral skin effect. In Sec. III, we establish the non-Hermitian chiral

*These authors contributed equally to this work.
†Corresponding author: spkou@bnu.edu.cn

skin effect theory using a low-energy effective model of chiral edge states. In Sec. IV, we list three non-Hermitian Haldane models, providing detailed descriptions of corresponding Hamiltonian. Secs. V–VII explore the physical properties of three non-Hermitian Haldane models, respectively. Moreover, in Sec. VIII, we introduce a circuit design capable of implementing the non-Hermitian chiral skin effect in the Haldane model. Finally, we conclude our work in Sec. IX.

## II. THEORETICAL ANALYSIS OF BOUNDARY CONDITIONS OF TOPOLOGICAL EDGE STATES

Firstly, we review the physical properties of traditional non-Hermitian skin effects. For traditional non-Hermitian skin effects, the bulk states exhibit extended under PBC, while they become exponentially localized at certain system boundaries under OBC. Therefore there exists a *PBC-OBC correspondence*, i.e.,

$$\text{extended states under PBC} \Leftrightarrow \text{localized states under OBC.}$$

Consider a 1D traditional non-Hermitian skin effect with a nonreciprocal model. The energy spectra exhibit loops under PBC and linear structures under OBC. A generalized Brillouin Zone is required to describe the spectra and wave functions under OBC, distinct from PBC. The non-Hermitian skin effect is identified by a corresponding "*winding number*", linked to point-gap topology, guaranteeing its existence [39,40].

Let us turn to the issue of non-Hermitian skin effect in topological edge states. We take topological edge states in 2D Chern insulators as an example.

In 2D Chern insulators, topological edge states exhibit specific chirality, meaning that they can only propagate along the boundary or interface of the system in one direction. Due to the influence of topological properties, electrons in these systems can only move in one direction and cannot propagate backward. For convenience in the subsequent discussions, we define the coordinate of any point on the irregular system's external boundary as $x$. The properties of chiral edge states on the boundary, such as their energy and effective dissipation, can be represented using a 1D coordinate system with $x$ as the coordinate. In general, to characterize the physical properties of the topological edge states, we project the original Hamiltonian of the 2D Chern insulator $\hat{H}_{2D}$ to that of edge states, $h_{\text{edge}}(x) = \hat{\mathcal{P}}_x \hat{H}_{2D} \hat{\mathcal{P}}_x$. Here, $\hat{\mathcal{P}}_x$ is a projection operator that projects the original 2D Hamiltonian to a 1D Hamiltonian of topological edge states by reducing the Hilbert space.

In particular, traditional PBC and OBC have significant limitations on characterizing chiral edge states because chiral edge states do *not* have open boundaries, and the boundaries are always closed. We introduce closed boundary conditions (CBC) to describe the boundary conditions for topological edge states. Under CBC, the wave function of topological edge states $\psi_{\text{edge}}$ satisfies $\psi_{\text{edge}}(0) = e^{i\phi}\psi_{\text{edge}}(L)$, where $\phi$ is the effective flux and $L$ is the length of the edge. To define CBC, we use the following equation:

$$|\psi_{\text{edge}}(0)| = |\psi_{\text{edge}}(L)|. \tag{1}$$

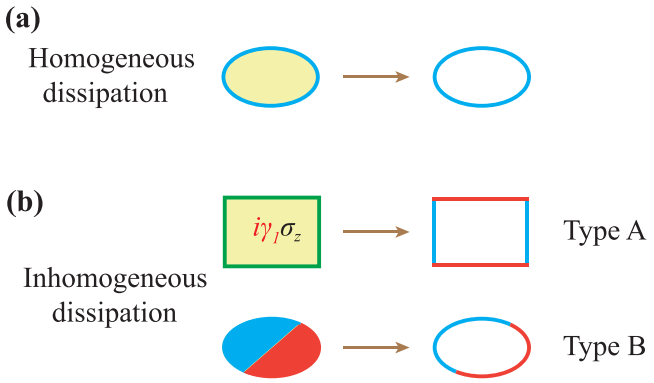


FIG. 1. (a) The illustration of a system with homogeneous dissipation under CBC. (b) The illustration of type A and type B domain walls under CBC in the system with inhomogeneous dissipation.

If we consider the dissipation, the effective Hamiltonian of topological edge states $h_{\text{edge}}(x)$ may become non-Hermitian, i.e., $h_{\text{edge}}(x) \neq h^{\dagger}_{\text{edge}}(x)$. In general, we have $\text{Im}(h_{\text{edge}}(x)) = \gamma(x)$. Under CBC, for the case of homogeneous dissipation, we have a uniform dissipation for topological edge states, i.e., $\gamma(x) \equiv$ constant or $\frac{d\gamma(x)}{dx} \equiv 0$; under CBC, for the case of inhomogeneous dissipation, we have a spatial-dependent dissipation for topological edge states, $\frac{d\gamma(x)}{dx} \neq 0$. Under CBC, the skin effect of topological edge states only arises in the presence of inhomogeneous dissipation. Moreover, the localized position is not at the system's "corner" but rather at the domain walls of dissipation on the closed boundary. The case of homogeneous dissipation is equivalent to PBC for traditional non-Hermitian skin effect, and the case of inhomogeneous dissipation with domain walls is similar to the case of OBC for traditional non-Hermitian skin effect.

Considering previous research and the work presented in this paper, we classify the domain walls into two types: type A and type B domain walls, based on CBC and dissipation distributions. This classification is essential for understanding the skin effect of topological edge states. For a visual representation, refer to the illustration in Fig. 1.

(1) Type A domain wall is defined as a system that adheres to traditional OBC, meaning it possesses lattice structures identical to those under PBC but is truncated into various geometric shapes with finite size. In this scenario, specific constraints arise due to the system's symmetry. As shown in Fig. 1(b), in the system with a rectangular boundary shape, under central symmetry, the effective dissipation of chiral edge states exhibits a staggered pattern under closed boundary conditions.

(2) Type B domain wall is defined as a system that deviates from traditional OBC. It involves interface problems between two distinct lattice models with different gain/loss or dissipation characteristics. As shown in Fig. 1(b), this system is created by splicing two 2D Chern insulators with different gain/loss. In this scenario, the effective dissipation of chiral edge states under closed boundary in real space is half gain and half loss.

To rigorously classify the two types of domain walls, we provide their mathematical definitions.

*Definition 1.* If a system can be divided into two regions with translationally invariant 2D Hamiltonian $\hat{H}^I_{2D}$ and $\hat{H}^{II}_{2D}$ by a dividing line, this line is defined as a domain wall. The domain wall separates two fragments of topological edge states described by effective Hamiltonian $h^I_{\text{edge}} = \hat{\mathcal{P}}_x \hat{H}^I_{2D} \hat{\mathcal{P}}_x$ and $h^{II}_{\text{edge}} = \hat{\mathcal{P}}_x \hat{H}^{II}_{2D} \hat{\mathcal{P}}_x$. In the case where $h^I_{\text{edge}} = h^{II}_{\text{edge}}$, it belongs to type A domain walls, signifying the system's translational invariance; Conversely, for $h^I_{\text{edge}} \neq h^{II}_{\text{edge}}$, it belongs to type B domain walls, indicating the system lacks translational invariance.

As a result, the case of type A domain wall is just an issue of a projected 2D Chern insulator with OBC. While the type B domain wall under CBC of inhomogeneous dissipation does not belong to a usual boundary condition (not PBC or OBC) for topological edge states.

In the following parts, we will study the non-Hermitian skin effect of topological edge states using CBC, categorizing them as type A and type B domain walls. By establishing a low-energy continuum effective model of 1D chiral edge states with inhomogeneous, perturbative dissipation, we reveal the mechanism of topological skin effect: chiral edge states under CBC exhibit skin effects in the presence of inhomogeneous effective dissipation. Therefore for non-Hermitian skin effect of topological edge states, there exists a *homogeneous-inhomogeneous correspondence*, i.e.,

extended topological edge states
under CBC of homogeneous dissipation
$\Leftrightarrow$ localized topological edge states
under CBC of inhomogeneous dissipation
(type A or type B domain walls).

## III. NON-HERMITIAN CHIRAL SKIN EFFECT

In this section, we first show the key properties of the non-Hermitian chiral skin effect for chiral modes with inhomogeneous dissipation. We emphasize that the non-Hermitian chiral skin effect is a unique type of non-Hermitian skin effect under CBC.

In the continuous limit, the effective single-body Hamiltonian for chiral modes in low-energy physics becomes

$$h_{\text{chiral}} = vk, \tag{2}$$

where $v$ is the velocity of edge states, and $k$ is the wave vector of the chiral modes. There are two types of chiral modes, one with positive velocity $v > 0$, the other with negative velocity $v < 0$. Then, we consider the effect of dissipation, of which the effective strength is $\gamma$ ($\text{Im}\gamma \equiv 0$), and the effective Hamiltonian of chiral modes turns into

$$h_{\text{chiral}} = vk + i\gamma = v(k - ik_0), \tag{3}$$

where $k_0 = -\gamma/v$. There is a notable aspect of chiral modes that *dissipation plays the role of an imaginary wave vector* [47].

In general, chiral modes are realized as topologically protected edge states on the boundaries of a 2D Chern insulator. Therefore topological edge states are chiral modes under CBC.

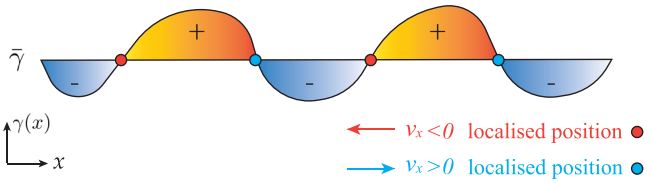


FIG. 2. The illustration of non-Hermitian chiral skin effect for chiral modes with inhomogeneous dissipation in the continuous limit. The red regions represent $\gamma_{\text{global}}(x) > 0$, and the blue regions represent $\gamma_{\text{global}}(x) < 0$. The red arrow and blue arrow represent the direction of Fermi velocity $v_x < 0$ and $v_x > 0$, respectively. The chiral edge states ($v_x < 0$) localized at the class-I global dissipation's domain walls $x_0^+$ (red dots), and the chiral edge states ($v_x > 0$) localized at the class-II global dissipation's domain walls $x_0^-$ (blue dots).

To answer the above questions, we consider a non-Hermitian Hamiltonian for chiral states with inhomogeneous, perturbative dissipation $\gamma(x)$ ($x \in [0, L]$, $|\gamma(x)| \ll 1$). Additionally, we establish CBC as $\psi(0) = e^{i\phi}\psi(L)$. The wave function in $x \in [0, L]$ is expressed as

$$\psi_k(x) = \frac{1}{\mathcal{N}} e^{ikx} e^{\frac{1}{v}\int_0^x [\gamma(x') - \bar{\gamma}]dx'}, \tag{4}$$

where $\mathcal{N}$ is a normalized coefficient, $k$ is the given wave number satisfying $k = (2\pi n + \phi)/L$ ($n \in \mathbb{Z}$), and $\bar{\gamma}$ is the average value of the integral of inhomogeneous dissipation in real space, given by

$$\bar{\gamma} = \frac{1}{L}\int_0^L \gamma(x)dx. \tag{5}$$

The energy levels for chiral modes become

$$E_{\text{chiral}} = vk + i\bar{\gamma}. \tag{6}$$

Equations (4) and (6) are derived in Appendix A. Before discussing the non-Hermitian chiral skin effect, we introduce *global dissipation* and its topological defects—*global dissipation's domain wall*.

*Definition 2.* Global dissipation: Global dissipation is defined as $\gamma_{\text{global}}(x) = \gamma(x) - \bar{\gamma}$, where $\bar{\gamma}$ is the average value of inhomogeneous dissipation $\bar{\gamma} = \frac{1}{L}\int_0^L \gamma(x)dx$. The integral path is a closed loop along the boundary of the chiral edge state.

*Definition 3.* Global dissipation's domain walls: (1) If there exists $x_0^+$ that satisfies $\gamma_{\text{global}}(x_0^+ + 0^-) < 0$ and $\gamma_{\text{global}}(x_0^+ + 0^+) > 0$, we denote $x_0^+$ as class-I global dissipation's domain wall. (2) If there exists $x_0^-$ that satisfies $\gamma_{\text{global}}(x_0^- + 0^-) > 0$ and $\gamma_{\text{global}}(x_0^- + 0^+) < 0$, we denote $x_0^-$ as class-II global dissipation's domain wall.

As shown in Fig. 2, the class-I global dissipation's domain walls represent red dots, and class-II global dissipation's domain walls represent blue dots. To determine the positions $x_0^\pm$ according to Definitions 1 and 2, it is necessary to integrate the inhomogeneous dissipation over the closed loop along the boundary of the chiral edge state to obtain $\bar{\gamma}$. This is why we refer to it as the "global " dissipation's domain wall. Furthermore, this highlights that the non-Hermitian chiral skin effect is a type of non-Hermitian skin effect specifically under

CBC. Subsequently, we present the critical properties of the non-Hermitian chiral skin effect.

*Definition 4.* The wave function is defined as localized at $x_0^{\pm}$ within the interval $[a, b]$, if the squared modulus of the wave function is monotonically increasing in the interval $[a, x_0^{\pm})$ and monotonically decreasing in the interval $(x_0^{\pm}, b]$.

*Theorem.* If $\gamma_{\text{global}}(x)$ is a continuous function, then a chiral mode with the negative speed is localized at $x_0^+$ (within a certain interval) if and only if there exists a class-I global dissipation's domain wall at $x_0^+$. Furthermore, a chiral mode with the positive speed is localized at $x_0^-$ (within a certain interval) if and only if there exists a class-II global dissipation's domain wall at $x_0^-$.

We show detailed proofs and examples in Appendixes B and C.

This result gives rise to an interesting effect, the non-Hermitian chiral skin effect, signifying the existence of the non-Hermitian skin effect for chiral modes under CBC. Global dissipation in real space plays the role of an "order parameter" characterizing the non-Hermitian chiral skin effect. The inhomogeneous effective dissipation under CBC indicates the presence of a non-Hermitian chiral skin effect. The zero points of inhomogeneous effective dissipation are called global dissipation's domain walls, where chiral edge states become localized.

In the following parts, the non-Hermitian chiral skin effect for homogeneous-inhomogeneous correspondence is applied to the topologically protected edge states in 2D Chern insulators with inhomogeneous dissipation. With the help of this toy lattice model, an additional property of non-Hermitian chiral skin effect—"*anomaly*" will be demonstrated.

## IV. MODEL

In this section, we consider chiral modes on the boundary of the non-Hermitian Haldane model with inhomogeneous, perturbative dissipation to describe the properties of the non-Hermitian chiral skin effect. The Haldane model is a typical model of a 2D Chern insulator on a honeycomb lattice [70,71], of which the Hamiltonian is

$$\hat{H}_{\text{haldane}} = t_1 \sum_{\langle ij \rangle} c_i^{\dagger} c_j + t_2 \sum_{\langle\langle ij \rangle\rangle} e^{i\phi_{ij}} c_i^{\dagger} c_j, \tag{7}$$

where $c_i^{\dagger}$ and $c_i$ are creation and annihilation operators for a particle at the $i$-th site. $\langle i, j \rangle$ and $\langle\langle i, j \rangle\rangle$ denote the nearest-neighbor hopping and the next-nearest-neighbor hopping, and $t_1$ and $t_2$ are the strength of nearest-neighbor hopping and next-nearest-neighbor hopping, respectively. $e^{i\phi_{ij}}$ is the complex phase of the next-nearest-neighbor hopping, and we set the direction of the positive phase as clockwise ($|\phi_{ij}| = \frac{\pi}{2}$). In this paper, we set $t_1$ to be a unit, and $t_2$ to be constant, i.e., $t_2 \equiv 0.2t_1$.

The topological characterization of the Haldane model is captured by the Chern number $Q$. Due to the existence of nonzero Chern number $Q = 1$, topological edge states are propagating along the system's edges, as shown in Fig. 3. For a system with PBC along $x$ direction, and an OBC along $y$ direction with zigzag edges, the effective Hamiltonian of topological edge states on one edge becomes

$$h_{\text{edge}}(k_x) = v_{\text{eff}} \sin k_x, \tag{8}$$

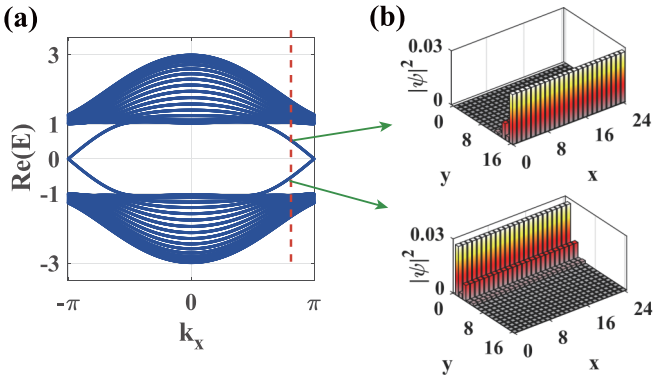


FIG. 3. (a) The energy dispersion in Hermitian Haldane model with zigzag edges. (b) The topological edge states in the Hermitian Haldane model.

where $k_x \in [\pi - k_0, \pi + k_0]$ and $v_{\text{eff}}$ represents the Fermi velocity. For the case of $t_2 = 0.2t_1$, we have $k_0 = 0.56\pi$, the details of $k_0$ can be found in Appendix D. Near Fermi surface with almost linear energy dispersion, the low-energy continuum Hamiltonian can be reduced to $h_{\text{edge}}(k_x) = v_{\text{eff}} k_x$, the topological edge states of such a Chern insulator are chiral modes.

To illustrate the non-Hermitian chiral skin effect, we consider a non-Hermitian Haldane model with inhomogeneous, perturbative dissipation. The Hamiltonian becomes

$$\hat{H}_{\text{total}} = \hat{H}_{\text{haldane}} + \delta\hat{H}_{\text{D}}, \tag{9}$$

where $\delta\hat{H}_{\text{D}}$ represents the term associated with dissipation. As shown in Fig. 4, in the subsequent sections, we investigate the non-Hermitian chiral skin effect for three cases of $\delta\hat{H}_{\text{D}}$: (a) staggered on-site gain/loss (Sec. V), (b) bulk dissipation (Sec. VI), and (c) dissipation on a single outermost zigzag edge (Sec. VII).

Considering the definition of domain walls presented in Sec. II with the non-Hermitian Haldane model depicted in Fig. 4, for inhomogeneous systems with translational symmetry where $\hat{H}_{2D}^{I} = \hat{H}_{2D}^{II}$, OBC in case (a) correspond to the CBC of type A domain walls. Moreover, for inhomogeneous systems without translational symmetry where $\hat{H}_{2D}^{I} \neq \hat{H}_{2D}^{II}$,

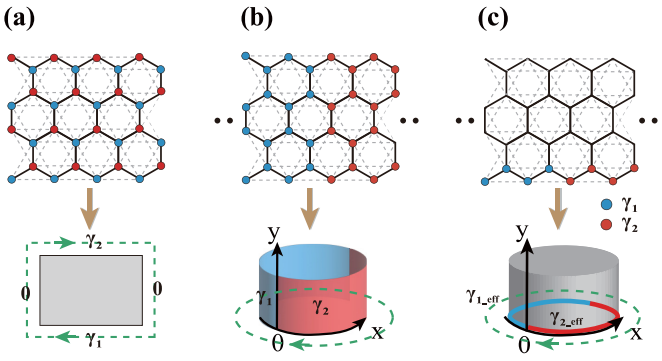


FIG. 4. Three different distributions of dissipation in the non-Hermitian Haldane models. (a) Staggered on-site gain/loss (Sec. V), (b) bulk dissipation (Sec. VI), and (c) dissipation on a single outermost zigzag edge (Sec. VII).

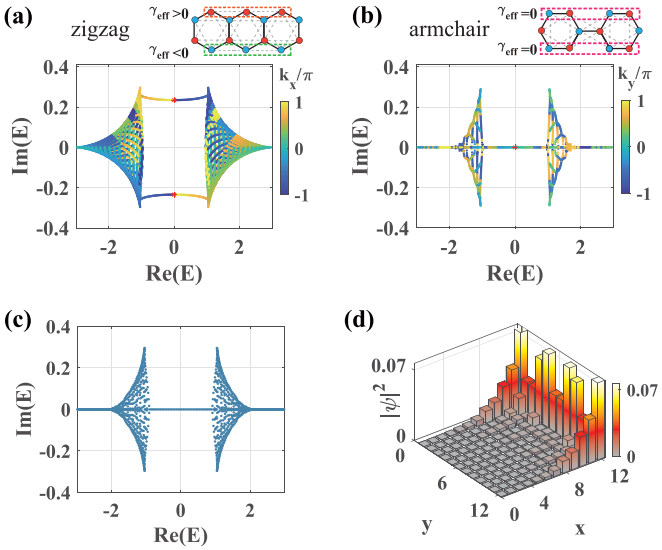


FIG. 5. [(a) and (b)] The complex spectra of the non-Hermitian Haldane model with (a) zigzag edges and (b) armchair edges. The orange boxes represent regions of effective gain, the green boxes represent regions of effective loss, and the magenta boxes represent regions without dissipation. (c) The complex spectrum of the non-Hermitian Haldane model under OBC with rectangular borders. It is equivalent to CBC of type A domain walls for topological edge states. (d) Spatial distribution of particles of the topological edge states in (c). The strength of gain/loss is $|\gamma| = 0.3t_1$.

cases (b) and (c) are associated with CBC of type B domain walls.

## V. APPLICATION: MECHANISM OF HYBRID SKIN-TOPOLOGICAL EFFECT IN CHERN INSULATORS

In this section, we explain the mechanism of the gain/loss-induced hybrid skin-topological effect and demonstrate that it can be understood by multiple global dissipation's domain walls for topological edge states in the theory of non-Hermitian chiral skin effect. Firstly, we focus on the non-Hermitian Haldane model, and the staggered on-site gain/loss can be expressed as [63]

$$\delta\hat{H}_{\mathrm{D}} = i\gamma \sum_i c^{\dagger}_{A,i}c_{A,i} - i\gamma \sum_i c^{\dagger}_{B,i}c_{B,i}, \tag{10}$$

where A/B are the two sublattice sites in each subcell, and $\gamma$ denotes the strength of dissipation.

In our study, the non-Hermitian chiral skin effect is the origin of the hybrid skin-topological effect, which arises from the presence of global effective dissipation at the boundaries. Next, we will demonstrate that staggered on-site gain/loss throughout the entire system can be equivalently regarded as effective dissipation at the boundaries for topological edge states.

To obtain the effective dissipation at each boundary, we consider two scenarios of the semi-infinite Haldane model under staggered dissipation: zigzag boundaries and armchair boundaries, as depicted in Figs. 5(a) and 5(b). The two scenarios are equivalent to CBC with effective homogeneous dissipation on the edge for topological edge states. The effective edge dissipation with zigzag edges for topological edge states is given by

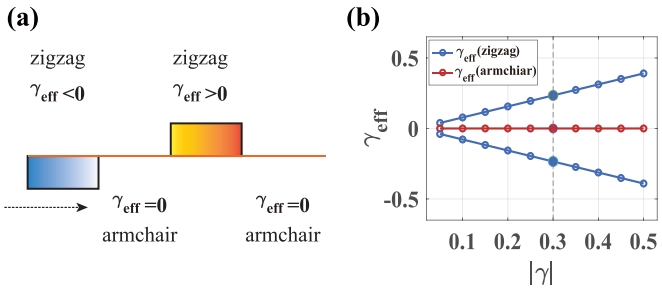


FIG. 6. (a) Schematic diagram illustrating multiglobal dissipation's domain walls, equivalent to non-Hermitian Haldane model with rectangular borders. The dotted arrows indicate the direction of the chiral edge states. (b) Variation of effective edge dissipation on the zigzag and armchair edges for varying strengths of $\gamma$.

$$\gamma_{\mathrm{eff}}^{\mathrm{zigzag}} = \mathrm{Im}\langle\psi_{\mathrm{edge}}(k_x)|\left(i\gamma \sum_i c^{\dagger}_{A,i}c_{A,i} - i\gamma \sum_i c^{\dagger}_{B,i}c_{B,i}\right)|\psi_{\mathrm{edge}}(k_x)\rangle, \tag{11}$$

and the effective edge dissipation with armchair edges for topological edge states is given by

$$\gamma_{\mathrm{eff}}^{\mathrm{armchair}} = \mathrm{Im}\langle\psi_{\mathrm{edge}}(k_y)|\left(i\gamma \sum_i c^{\dagger}_{A,i}c_{A,i} - i\gamma \sum_i c^{\dagger}_{B,i}c_{B,i}\right)|\psi_{\mathrm{edge}}(k_y)\rangle, \tag{12}$$

where $\psi_{\mathrm{edge}}$ denote topological edge states. In the simplest case, when both the system and dissipation exhibit sublattice symmetry, the effective edge dissipation of topological edge states can be inferred from the imaginary parts of energy eigenvalues with zero real parts in the complex spectra, as indicated by the red stars in Figs. 5(a) and 5(b).

Moreover, when the system has a rectangular boundary under OBC with two zigzag-shaped and two armchair-shaped edges, it corresponds to type A domain walls under CBC. The energy spectrum and the wave functions of the topological edge states, in this case, are illustrated in Figs. 5(c) and 5(d), respectively.

As previously discussed, chiral edge states are determined by the effective dissipation on the system's geometric boundaries. To explain the mechanism of the hybrid skin-topological effect, we map the system under OBC with the rectangular boundary to the multiglobal dissipation's domain walls in the framework of the non-Hermitian chiral skin effect. As shown in Fig. 6(a), the system with rectangular borders can be transformed into the multiglobal dissipation's domain walls. And the effective dissipation along the four edges can be obtained as shown in Fig. 6(b), corresponding to $-\gamma_{\mathrm{eff}}^{\mathrm{zigzag}}$, 0, $\gamma_{\mathrm{eff}}^{\mathrm{zigzag}}$, and 0. By analyzing the multiglobal dissipation's domain walls, we explain the wave function of topological edge states in Fig. 5(d). In Fig. 6(a), the direction of chiral current is positive ($v > 0$), based on Eq. (4) and

continuity condition at each global dissipation's domain wall, the wave function increases along the $x$-axis in the region where $\gamma_{\text{eff}} - \bar{\gamma} > 0$, decreases in the region where $\gamma_{\text{eff}} - \bar{\gamma} < 0$, and extended in the region where $\gamma_{\text{eff}} - \bar{\gamma} = 0$. As a result, Fig. 5(d) shows the extension of chiral edge states at the armchair boundary, where the effective dissipation is zero. Conversely, at the zigzag boundary, the chiral edge states exhibit localization in a specific direction, indicative of the skin effect. Further detailed derivations for the solutions of the multiglobal dissipation's domain walls model can be found in Appendix E.

In summary, we conclude that the non-Hermitian chiral skin effect is the mechanism behind the hybrid skin-topological effect in Chern insulators, distinguishing it from the non-Hermitian skin effect in 1D model or higher-order non-Hermitian skin effect. Our findings demonstrate that the hybrid skin-topological effect can be understood by introducing inhomogeneous effective dissipation at the system boundaries.

## VI. NON-HERMITIAN CHIRAL SKIN EFFECT FOR BULK DISSIPATION DOMAIN WALLS

Now, we consider bulk dissipation on the Haldane model, i.e.,

$$\delta\hat{H}_{\text{D}} = i\sum_{\text{bulk}} \gamma_i c_i^\dagger c_i, \tag{13}$$

where $\gamma_i$ represents the strength of dissipation at the $i$-th lattice site among all lattice sites. Firstly, we discuss the Haldane model with uniform bulk dissipation, $\gamma_i = \gamma$. When $\gamma \neq 0$, the imaginary parts of energy levels $E(k_x, y)$ in the complex spectrum have a global, uniform, shift,

$$\text{Im}E(k_x, y) = 0 \rightarrow \text{Im}E(k_x, y) \equiv \gamma. \tag{14}$$

The dispersion relation of one edge mode is given by

$$h_{\text{edge}}(k_x) = v_{\text{eff}} \sin k_x + i\gamma. \tag{15}$$

In continuous limit, near $k_x = \pi$, $h_{\text{edge}}(k_x)$ is reduced into Eq. (3), i.e.,

$$h_{\text{edge}}(k_x) \simeq v_{\text{eff}}(\Delta k + i(\gamma/v_{\text{eff}})), \tag{16}$$

where $\Delta k = k_x - \pi$. Therefore this homogeneous case looks trivial.

Next, to verify the existence of the non-Hermitian chiral skin effect, we discuss the Haldane model in the cylinder geometry ($x$PBC/$y$OBC) with inhomogeneous bulk dissipation by considering a pair of global dissipation's domain walls in bulk, which is equivalent to CBC of type B domain wall for topological edge states. As shown in Figs. 7(a) and 7(b), the cases where there is a difference in the bulk's dissipation between the left and right regions are investigated. In both models, we show the existence of a non-Hermitian chiral skin effect—the energy levels of topological edge states become a line in the complex energy spectra [Figs. 7(a) and 7(b)] and the topological edge states accumulate around the global dissipation's domain walls [Fig. 7(c)]. In addition, the numerical results match our analytical prediction based on Eq. (15)

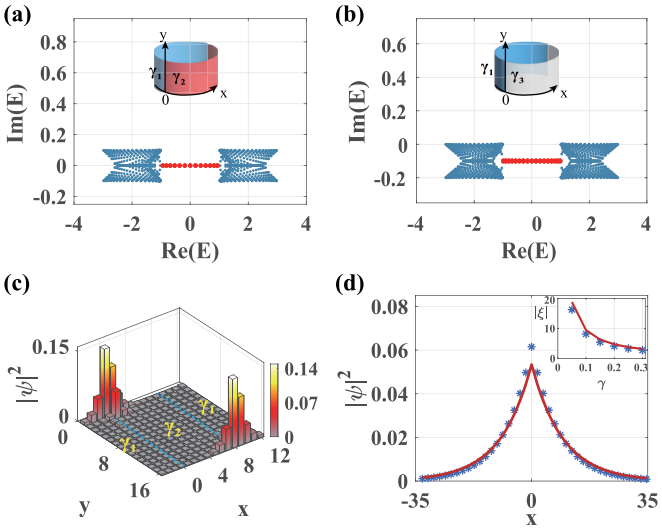


FIG. 7. Non-Hermitian Haldane model in the cylinder geometry ($x$PBC/$y$OBC) with global dissipation's domain walls in bulk, equivalent to CBC of type B domain wall for topological edge states. [(a) and (b)] The complex spectra with global dissipation's domain walls (a) $\gamma_1 = -0.1t_1, \gamma_2 = 0.1t_1$ and (b) $\gamma_1 = -0.2t_1, \gamma_2 = 0$. The blue and red dots represent the energy levels of bulk and topological edge states, respectively. (c) Particle distribution of the topological edge states. The dissipation is set as $\gamma_2(0 < x < 8) = 0.2t_1, \gamma_1(-4 < x < 0, 8 < x < 12) = -0.2t_1$. (d) Comparison between numerical results (blue stars) and theoretical predictions (red line) of the particle distribution of a topological edge state at the edge ($y = 0$). The inset displays the localization length $\xi$ for varying strengths of $\gamma$. The numerical results are obtained from the non-Hermitian Haldane model, while the theoretical results are derived from Eq. (17). Both wave functions are normalized along the $x$ direction.

[Fig. 7(d)]. The localization length $\xi$ becomes

$$\xi = \frac{v_{\text{eff}}}{\gamma}, \tag{17}$$

and the specific derivations can be found in Appendix C.

In summary, such non-Hermitian chiral skin effect can never be characterized by certain pointlike topology configurations in the complex spectrum or corresponding "winding number"! Instead, it is global dissipation $\gamma_{\text{global}}$ that can characterize the strength of the non-Hermitian chiral skin effect.

## VII. NON-HERMITIAN CHIRAL SKIN EFFECT FOR EDGE DISSIPATION DOMAIN WALLS

We then consider the effect of inhomogeneous dissipation on the single outermost zigzag edge, i.e.,

$$\delta\hat{H}_{\text{D}} = i\sum_{\text{lower-edge}} \gamma_i c_i^\dagger c_i. \tag{18}$$

### A. Effective model for topological edge states: fractional Hatano-Nelson model

First, we point out that *the effective model for topological edge states in this condition is a fractional Hatano-Nelson model that could exactly characterize non-Hermitian chiral skin effect*. The effective Hamiltonian for the topological edge

states on the lower edge is given by

$$h_{\text{edge}}(k_x) = v_{\text{eff}} \sin k_x + i\gamma_{\text{eff}}, \tag{19}$$

where $k_x = \pi + \Delta k$. And $\gamma_{\text{eff}}$ represents the effective dissipation, defined as

$$\gamma_{\text{eff}} = \text{Im}\langle\psi_{\text{edge}}|\hat{H}_{\text{total}}|\psi_{\text{edge}}\rangle. \tag{20}$$

where $\psi_{\text{edge}}$ denotes the wave functions of the chiral modes.

To accurately characterize the non-Hermitian chiral skin effect, we obtain the effective Hamiltonian for topological edge states by data fitting the effective dissipation for a uniform case $\gamma_i = \gamma$. Now, we have

$$\gamma_{\text{eff}}(k_x) = \sum_n a_n \cos nk_x. \tag{21}$$

For example, in the case of $\gamma = 0.1t_1$, we have $a_1 \simeq 0.12t_1$, $a_2 \simeq 0.023t_1$. As a result, the effective Hamiltonian for chiral edge states $h_{\text{edge}}(k_x)$ with uniform edge dissipation becomes a 1D Hatano-Nelson model described by

$$h_{\text{edge}}(k_x) = h_{\text{fractional-HN}}(k_x) \simeq v_{\text{eff}} \sin k_x + i\gamma_{\text{eff}}(k_x),$$
$$k_x \in (\pi - k_0, \pi + k_0], \tag{22}$$

where $\gamma_{\text{eff}}(k_x) = a_1 \cos k_x + a_2 \cos 2k_x$. For clarity, we map Eq. (22) to the usual 1D generalized Hatano-Nelson model, we have

$$\hat{H}_{\text{HN}} = \sum_i (t_L c_i^\dagger c_{i+1} + t_R c_{i+1}^\dagger c_i)$$
$$= \sum_{k_x \in (-\pi,\pi)} a_{k_x}^\dagger (v_{\text{eff}} \sin k_x + i\zeta \cos k_x) a_{k_x}, \tag{23}$$

where $t_L = (v_{\text{eff}} - \zeta)/2$ and $t_R = (v_{\text{eff}} + \zeta)/2$. According to the 1D Hatano-Nelson model, the localization length in non-Hermitian Haldane model is described by

$$\xi = \frac{c}{2 \ln \frac{v_{\text{eff}}+\zeta}{v_{\text{eff}}-\zeta}}, \tag{24}$$

where $c = \sqrt{3}a$ and $a$ is lattice constant of Haldane model.

In particular, due to $k_0 \neq \pi$, the 1D Hatano-Nelson model is fractionalized. To characterize the fractional Hatano-Nelson model $h_{\text{fractional-HN}}(k_x)$, we use the fraction $\nu = \frac{k_0}{\pi}$ to denote the "*anomaly*" of the non-Hermitian chiral skin effect of topological edge states. For example, for the case of $t_2 = 0.2t_1$, we have the fraction of anomaly $\nu = \frac{k_0}{\pi} = 0.56$, and the details regarding the derivation of $\nu$ can be found in Appendix D. Now, we have a 1D fractional-Hatano-Nelson model $h_{\text{fractional-HN}}(k_x)$.

The characteristics of the complex spectra under edge dissipation are discussed. The numerical results given by the non-Hermitian Haldane model match the fractional Hatano-Nelson model $h_{\text{fractional-HN}}(k_x)$. As shown in Fig. 8(a), the red line represents the numerical energy levels of the topological edge states under PBC and the cobalt blue stars represent the numerical energy levels of the 1D Hatano-Nelson model. By comparing the energy levels, it is found that the effective model of chiral modes at $y = 0$ is a fractional Hatano-Nelson model $h_{\text{fractional-HN}}(k_x)$, which is the negative imaginary parts of the energy levels of the 1D Hatano-Nelson model. Moreover, as shown in Fig. 8(d), the numerical results of the particle distribution of topological edge states match our analytical prediction based on Eq. (22). The inset in Fig. 8(d) illustrates that the numerical results for the localization length $\xi$ presented in Eq. (24) correspond to the localization length of the fractional Hatano-Nelson model $h_{\text{fractional-HN}}(k_x)$.

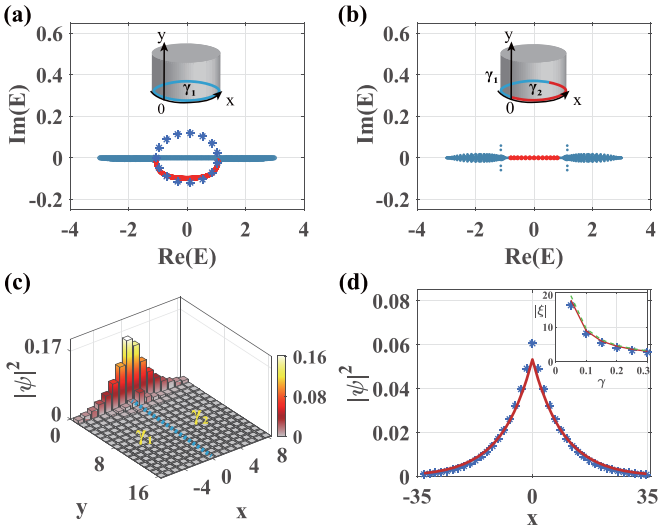


FIG. 8. Non-Hermitian Haldane model in the cylinder geometry ($x$PBC/$y$OBC) with dissipation on a single outermost zigzag edge ($y = 0$), which is is equivalent to CBC of type B domain wall for topological edge states. [(a) and (b)] Complex spectra with (a) uniform dissipation $\gamma_1 = -0.1t_1$ and (b) global dissipation's domain wall ($\gamma_1 = -0.1t_1, \gamma_2 = 0.1t_1$). Blue dots, red dots, and cobalt blue stars represent energy levels of bulk states, topological edge states in the non-Hermitian Haldane model, and energy levels of the effective 1D Hatano-Nelson model [Eq. (22)], respectively. (c) Particle distribution of topological edge states. The global dissipation's domain wall is set as $\gamma_2(x > 0) = 0.2t_1$, $\gamma_1(x < 0) = -0.2t_1$. (d) Comparison between numerical and theoretical results for the particle distribution of topological edge states at $y = 0$. The inset shows the localization length $\xi$ for varying dissipation strengths $\gamma$. Blue stars, red lines, and green dash lines represent numerical results for the non-Hermitian Haldane model, theoretical results for the half Hatano-Nelson model [Eq. (24)], and continuous limits [Eq. (17)]. Both wave functions are normalized along the $x$ direction.

The localization behavior of topological edge states under edge dissipation is investigated using the non-Hermitian chiral skin effect. Firstly, we introduce uniform dissipation on the outermost edge at $y = 0$ with $\gamma_i = -0.1t_1$, as shown in Fig. 8(a). The complex spectrum reveals that the chiral edge states on the dissipative edge exhibit nonzero effective dissipation. Next, we consider an asymmetric dissipation configuration on the outermost edge ($y = 0$), where one-half of the system has dissipation $\gamma_1(x < 0) = -0.1t_1$. The other half has dissipation $\gamma_2(x > 0) = 0.1t_1$, as depicted in Fig. 8(b). By utilizing the theory of non-Hermitian chiral skin effect, we predict the emergence of class-I global dissipation's domain walls on the dissipative edge at $x = 0$, which are associated with the direction of chiral current $v_x < 0$ at the edge $y = 0$. The numerical results of the particle distribution, as depicted in Fig. 8(c), confirm the localization of chiral edge states at the class-I global dissipation's domain walls, thus validating the theoretical predictions.

Therefore non-Hermitian chiral skin effect can be considered as "*anomaly*" non-Hermitian skin effect and only is

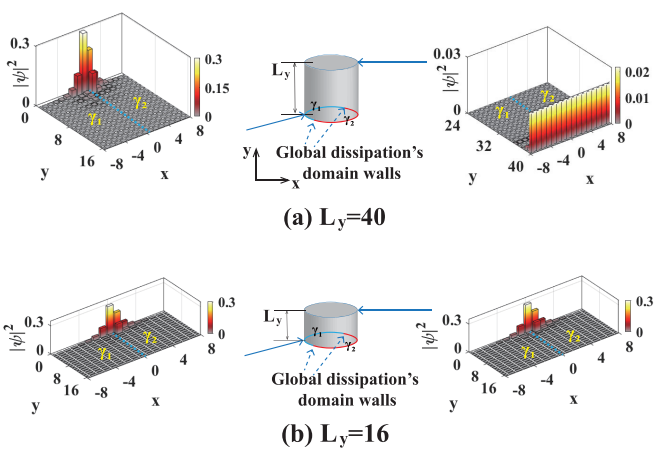


FIG. 9. The nonlocal effect of non-Hermitian chiral skin effect. The nanoribbons of the Haldane model with a pair of global dissipation's domain wall on a single outermost zigzag edge ($y = 0$) ($\gamma_2(x > 0) = 0.5t_1$, $\gamma_1(x < 0) = -0.5t_1$). (a) The topological edge states on edge ($y = 0$) are localized on the global dissipation's domain wall, and the other on edge ($y = L_y$) are extended on its corresponding edge. (b) The topological edge states on both edges ($y = 0$, $y = L_y$) are localized on the global dissipation's domain wall.

realized on the global dissipation's domain walls of a 2D Chern insulator.

### B. Nonlocal effect of non-Hermitian chiral skin effect

Second, we discuss the interplay between the topological edge states on both edges (the edge with dissipation and that without) and show the nonlocal effect of non-Hermitian chiral skin effect. We consider a non-Hermitian Haldane model on a strip with zigzag edges, of which one edge has dissipation ($y = 0$) and the other has not ($y = L_y$). The distance between two edges is set to be $L_y$, as shown in Fig. 9(a).

We consider the global dissipation's domain walls on the edge ($y = 0$). In the limit of $L_y \to \infty$ (for example, $L_y = 40$), the results look trivial—due to non-Hermitian chiral skin effect, the topological edge states on the edge with global dissipation's domain walls become localized on global dissipation's domain walls; the topological edge states on the edge without dissipation are extended, as shown in Fig. 9(a). In the scenario where $L_y$ has a small value (for example, $L_y = 16$), an unusual occurrence takes place whereby the topological edge states on the edge with dissipation as well as the ones on the edge without it *both* become localized on the same global dissipation's domain walls. To emphasize the results, we call it *nonlocal non-Hermitian chiral skin effect*, as shown in Fig. 9(b). In the future, we will study the mechanism for nonlocal non-Hermitian chiral skin effect and try to give a reasonable answer.

## VIII. REALIZATION OF AN ELECTRIC CIRCUIT IN HALDANE MODEL WITH GLOBAL DISSIPATION DOMAIN WALL

In this section, we present a circuit design that implements the non-Hermitian Haldane model with global dissipation's domain walls.

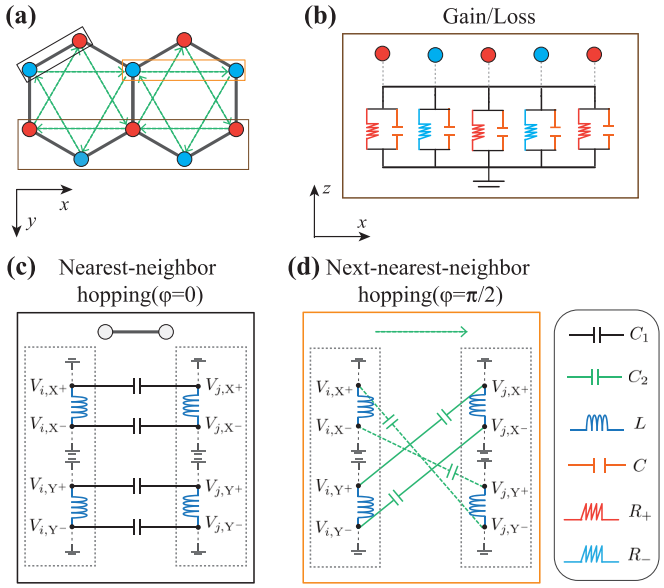


FIG. 10. The schematic of the designed electric circuit. (a) Illustration of non-Hermitian Haldane model. The brown box indicates the global dissipation's domain wall shown in (b), the black box indicates the nearest neighbor hopping shown in (c), and the orange box indicates the next-nearest-neighbor hoping shown in (d). (b) The circuit implementation of the global dissipation's domain wall. (c) Schematic of the circuit implementation of the nearest-neighbor hopping. (d) Schematic of the circuit implementation of the next-nearest-neighbor hopping.

Our experimental platform utilizes an LC circuit combined with resistors ($R_-$) and negative resistors (INIC) ($R_+$) to observe the non-Hermitian chiral skin effect in the non-Hermitian Haldane model with global dissipation's domain wall. To map the Haldane model with global dissipation's domain wall onto the electric circuit, we introduce various types of couplings [72,73] and on-site gain/loss [74]. Three charts in Fig. 10 illustrate the circuit implementations of nearest-neighbor hopping [Fig. 10(c)], next-nearest-neighbor hopping [Fig. 10(d)], and global dissipation's domain walls [Fig. 10(b)]. In Figs. 10(c) and 10(d), the gray dotted box represents a lattice site in a tight-binding model containing two inductors (X, Y). The voltages between the inductors denoted as $U_X$ and $U_Y$, are used to define the variables $U_{\uparrow,\downarrow} = U_X \pm iU_Y$. By applying Kirchhoff's law and utilizing this notation, we derive the eigenequation for the spin-up and spin-down states

$$E\begin{bmatrix} U^A_{\mathbf{k},\uparrow} \\ U^B_{\mathbf{k},\uparrow} \end{bmatrix} = \begin{bmatrix} p_k(\varphi) + i\gamma_A & T_{\mathbf{k}} \\ T^*_{\mathbf{k}} & p_k(-\varphi) + i\gamma_B \end{bmatrix}\begin{bmatrix} U^A_{\mathbf{k},\uparrow} \\ U^B_{\mathbf{k},\uparrow} \end{bmatrix}, \quad (25)$$

where the eigenfrequency of circuit is $\omega_0 = 1/\sqrt{LC}$, the energy is characterized by $E = 3t_1 + 6t_2 + 1 - \frac{2w_0^2}{w^2}$, the next-nearest-neighbor hopping is characterized by $p_{\mathbf{k}}(\varphi) = 2t_2[\cos(\mathbf{k}\cdot\mathbf{v_1} + \varphi) + \cos(\mathbf{k}\cdot\mathbf{v_2} + \varphi) + \cos(\mathbf{k}\cdot\mathbf{v_3} + \varphi)]$, the nearest-neighbor hopping is characterized by $T_{\mathbf{k}} = t_1(e^{i\mathbf{k}\mathbf{e}_1} + e^{i\mathbf{k}\mathbf{e}_2} + e^{i\mathbf{k}\mathbf{e}_3})$. Notably, the non-Hermitian term is described as

$$i\gamma_{A(B)} = \frac{i}{R_{g,A(B)}}\sqrt{\frac{L}{C}}. \quad (26)$$

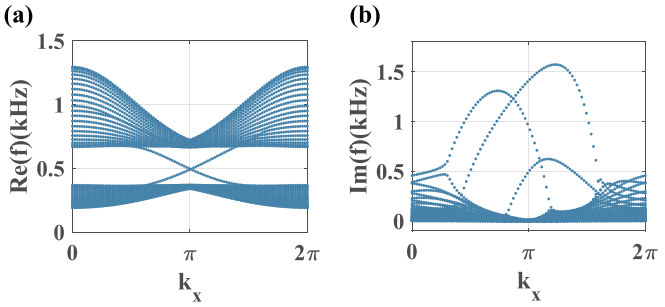


FIG. 11. Band structure of the circuit lattice ($x$PBC/$y$OBC) with dissipation on a single outermost zigzag edge. The circuit parameters are $L = 3.3\,\mathrm{mH}$, $C_1 = 3300\,\mathrm{pF}$, $C_2 = 660\,\mathrm{pF}$, and $R = 2\,\mathrm{k\Omega}$.

It is noted that $R_{g,A(B)}$ can be negative using INIC. We show more details in Appendix F. For convenience, the grounding capacitance is set as $C_g = C$, and capacitors representing coupling are set as $C_1 = t_1 C$ and $C_2 = t_2 C$. The specific derivations can be found in Appendix F.

Equation (25) is the eigefunction of the non-Hermitian Haldane model. Consider $E = \varepsilon(k)$ is the Hamiltonian's eigenvalues, and the frequency satisfy

$$f_k = \frac{1}{2\pi}\sqrt{\frac{2}{LC(3t_1 + 6t_2 + 1 - \varepsilon(k))}}, \tag{27}$$

where Fig. 11 shows the calculated band spectrum of the semi-infinite circuit lattice, with the vertical axis being frequency $f_k$. It agrees with the system in Fig. 8(a), which is a Chern insulator with homogeneous dissipation on a single zigzag edge.

Let us now consider the electric circuit that has PBC along the $x$ direction, and an OBC along the $y$ direction with zigzag edges, the nearest-neighbor and next-nearest-neighbor coupling is grounded at $y = 0$ and $y = L$. We utilize two approaches to achieve a pair of global dissipation's domain walls. In the first approach, we place half of the resistors with a value of $R_1$ and half of the resistors with a value of $R_2$ at the corresponding grid points on the boundary. Alternatively, in the second approach, we position half of the resistors with a value of $R_1$ and an equal number of the same type of INIC at the corresponding grid points on the boundary. These strategies enable us to create the global dissipation's domain wall and facilitate the desired dissipation distribution. In semi-infinite case, the voltage distribution at the eigenfrequency $\omega_0$ is measured to obtain the corresponding eigenvalue $E$ and the eigenstate $[U^A_{\mathbf{k},\uparrow}, U^B_{\mathbf{k},\uparrow}]^T$. These simulation experiments are convenient for observing the non-Hermitian chiral skin effect.

## IX. CONCLUSION

In summary, we conclude that

chiral modes under CBC + inhomogeneous dissipation

→ non-Hermitian chiral skin effect.

In the end, we answer the three questions at the beginning.

In response to the question (i), the non-Hermitian chiral skin effect represents a novel non-Hermitian skin effect. Firstly, there exists an anomaly in chiral edge states and it cannot be observed in a 1D lattice model. In our study, we introduce the concept of CBC to characterize the boundary conditions of chiral edge states. We define the localized positions of chiral edge states as generalized domain walls, classifying domain walls into types A and B. While type A domain walls have been extensively studied in previous research, and type B domain walls, being more controllable, become the central focus of our investigation.

TABLE I. The features of non-Hermitian chiral skin effect.

| Properties | Non-Hermitian chiral skin effect |
|---|---|
| Boundary condition | Closed boundary condition |
| Anomalous phenomenon | Cannot be observed in a 1D model |
| "Order parameter" | Global dissipation $\gamma_{\mathrm{global}}(x)$ |
| Localized position | Global dissipation's domain walls |

Secondly, an anomaly emerges in the energy spectrum of chiral edge states in both type A and type B domain walls. Notably, we emphasize the distinctive nature of type B domain walls. Under homogeneous dissipation, type B domain walls form a line structure in the complex energy spectrum. However, under inhomogeneous dissipation, it still retains its line structure while exhibiting skin effects. The phenomenon where homogeneous and inhomogeneous energy spectra both form line structures challenges the conventional bulk-boundary correspondence.

In response to the question (ii), we reveal the mechanism of the non-Hermitian chiral skin effect by establishing a low-energy continuous effective model of 1D chiral edge states under CBC with inhomogeneous and perturbative dissipation. Under CBC, chiral edge states exhibit non-Hermitian skin effects in the presence of inhomogeneous effective dissipation. We use two key concepts to describe this phenomenon: $\gamma_{\mathrm{global}}$ and global dissipation's domain wall. $\gamma_{\mathrm{global}}$ is used to describe the inhomogeneous dissipation in the system. We define the integral value of the dissipation on the closed boundary as a base value $\bar{\gamma}$, and $\gamma_{\mathrm{global}}$ is the difference between the dissipation on the closed boundary $\gamma(x)$ and the base value $\bar{\gamma}$. The zero points of $\gamma_{\mathrm{global}}$ define the position of the global dissipation's domain wall, which is the localization position of the chiral edge states. A comprehensive overview is presented in Table I.

In response to the question (iii), we verify the theory of non-Hermitian chiral skin effect using three non-Hermitian Haldane models with type A and type B domain walls. Our theory successfully explains the gain/loss-induced hybrid skin-topological effect and the newly discovered non-Hermitian chiral skin effect.

In the future, we will try to understand the interplay of systematically non-Hermitian physics and topological quantum states by studying the non-Hermitian chiral skin effect for topological edge states in other types of topological quantum states, such as higher-order Chern insulators, topological superconductors, and topological semimetals.

*Note added.* Recently, we noticed three related studies, including two theoretical studies [68,75] and an experimental study [69].

## ACKNOWLEDGMENTS

This work was supported by the Natural Science Foundation of China (Grants No. 11974053 and No. 12174030) and the National Key R&D Program of China (Grant No. 2023YFA1406704). We are grateful to Zhong Wang, Chen Fang, Lin-Hu Li, Wei Yi, Gao-yong Sun, Ya-jie Wu, Can Wang, Fei Yang, Xian-qi Tong, and Yue Hu for helpful discussions that contributed to clarifying some aspects related to the present work.


## APPENDIX A: THE WAVE FUNCTIONS OF CHIRAL EDGE STATES WITH DISSIPATION $\gamma(x)$

The effective edge model of the topological edge states is given by the Hamiltonian

$$\hat{H} = vk + i\gamma(x) \tag{A1}$$

or

$$\hat{H} = -iv\frac{d}{dx} + i\gamma(x), \tag{A2}$$

where $x \in [0, L]$, $v$ is the velocity of the edge states, $k$ is the wave number, and $\gamma(x)$ represents the dissipation as a function of position $x$.

To obtain the wave function of the topological edge states, we consider the stationary Schrödinger equation

$$\left[-iv\frac{d}{dx} + i\gamma(x)\right]\psi(x) = E\psi(x), \tag{A3}$$

where $E$ is the energy of the system. Solving this equation, we obtain the wave function

$$\psi(x) = \frac{1}{\mathcal{N}} e^{i\frac{E}{v}x} e^{\frac{1}{v}\int \gamma(x)dx}, \tag{A4}$$

where $\mathcal{N}$ is the normalization factor. Here, $E$ can be any complex number.

To determine the energy $E$, we impose CBC $\psi(0) = e^{i\phi}\psi(L)$, which yield

$$i\frac{E}{v}L + \frac{1}{v}\int_0^L \gamma(x)dx = i2\pi n + i\phi, \tag{A5}$$

where $n \in \mathbb{Z}$. This equation gives us the energy of the edge states, which can be expressed as

$$E = vk + i\bar{\gamma}, \tag{A6}$$

where $k = \frac{2\pi n+\phi}{L}$ and $\bar{\gamma} = \frac{1}{L}\int_0^L \gamma(x)dx$. Substituting this expression for $E$ into the wave function, we obtain

$$\psi_k(x) = \frac{1}{\mathcal{N}} e^{ikx} e^{\frac{1}{v}\int_0^x [\gamma(x)-\bar{\gamma}]dx}. \tag{A7}$$

This equation describes the wave function of the edge states for a given wave number $k$. We define global dissipation as $\gamma_{\text{global}}(x) = \gamma(x) - \bar{\gamma}$, where $\bar{\gamma}$ is the average value of inhomogeneous dissipation $\bar{\gamma} = \frac{1}{L}\int_0^L \gamma(x)dx$.

## APPENDIX B: PROOF OF THE RELATIONSHIP BETWEEN WAVE FUNCTION LOCALIZATION AND THE EXISTENCE OF GLOBAL DISSIPATION'S DOMAIN WALLS

*Definition 2.* $x_0$ is called the class-I global dissipation's domain wall on the interval $[a, b]$. We always make $a$ and $b$ belong to $[0, L]$ by changing the initial point, if there exist three positive real numbers, $a < x_0 < b$, such that for any $x_L$ satisfying $a < x_L < x_0$, $\gamma_{\text{global}}(x_L) < 0$, and for any $x_R$ satisfying $x_0 < x_R < b$, $\gamma_{\text{global}}(x_R) > 0$.

*Definition 3.* $x_0$ is called a class-II global dissipation's domain wall on the interval $[a, b]$. We always make $a$ and $b$ belong to $[0, L]$ by changing the initial point, if there exist three positive real numbers, $a < x_0 < b$, such that for any $x_L$ satisfying $a < x_L < x_0$, $\gamma_{\text{global}}(x_L) > 0$, and for any $x_R$ satisfying $x_0 < x_R < b$, $\gamma_{\text{global}}(x_R) < 0$.

*Definition 4.* The wave function is said to be localized at $x_0$ within the interval $[a, b]$ if the squared modulus of the wave function is monotonically increasing in the interval $[a, x_0)$ and monotonically decreasing in the interval $(x_0, b]$ when $a < x_0 < b$.

*Theorem.* If $\gamma_{\text{global}}(x)$ is a continuous function, then a chiral mode with a negative speed is localized at $x_0$ (within a certain interval) if and only if there exists a class-I global dissipation's domain wall at $x_0$. Furthermore, a chiral mode with a positive speed is localized at $x_0$ (within a certain interval) if and only if there exists the class-II global dissipation's domain wall at $x_0$.

*Proof.*

*Sufficiency:* We first prove that the existence of the class-I global dissipation's domain wall or a class-II global dissipation's domain wall implies the localization of the corresponding chiral mode.

Assume we have a class-I global dissipation's domain wall at $x_0$. According to Definition 2, for any $x_L$ satisfying $a < x_L < x_0$, we have $\gamma_{\text{global}}(x_L) < 0$, and for any $x_R$ satisfying $x_0 < x_R < b$, we have $\gamma_{\text{global}}(x_R) > 0$. The squared modulus of the wave function is

$$|\psi_k(x)|^2 = \frac{1}{\mathcal{N}^2} e^{\frac{2}{v}\int_0^x \gamma_{\text{global}}(x')dx'} > 0. \tag{B1}$$

We now find the derivative of the squared modulus for $x$. Based on Eq. (B1), due to $\gamma_{\text{global}}(x)$ is a continuous function, we obtain

$$\frac{d|\psi_k(x)|^2}{dx} = \frac{2}{v}|\psi_k(x)|^2\gamma_{\text{global}}(x). \tag{B2}$$

Since $\gamma_{\text{global}}(x_L) < 0$ and $\gamma_{\text{global}}(x_R) > 0$, according to Eq. (B2), we deduce that

$$\begin{aligned} &\text{sign}(v)\frac{d|\psi_k(x_L)|^2}{dx} < 0, \quad \text{in the interval } [a, x_0), \\ &\text{sign}(v)\frac{d|\psi_k(x_R)|^2}{dx} > 0, \quad \text{in the interval } (x_0, b]. \end{aligned} \tag{B3}$$

This means that for the chiral mode with a negative speed, the squared modulus is monotonically increasing in the interval $[a, x_0)$ and monotonically decreasing in the interval $(x_0, b]$. Thus, the chiral mode with negative speed will be localized at $x_0$.

Similarly, assume we have a class-II global dissipation's domain wall at $x_0$. According to Definition 3, for any $x_L$ satisfying $a < x_L < x_0$, we have $\gamma_{\text{global}}(x_L) > 0$, and for any $x_R$ satisfying $x_0 < x_R < b$, we have $\gamma_{\text{global}}(x_R) < 0$. Using the same arguments as before with the derivative of the squared modulus in Eq. (B2), we can conclude that the squared modulus is monotonically increasing in the interval $[a, x_0)$ and monotonically decreasing in the interval $(x_0, b]$. Consequently, the chiral mode with positive speed will be localized at $x_0$ provided we have a class-II global dissipation's domain wall.

*Necessity:* Now, we prove that the localization of chiral modes can only occur if there is a class-I or class-II global dissipation's domain wall.

Assume a chiral mode with negative speed is localized at $x_0$. Based on Definition 4, the squared modulus of the wave function should be monotonically increasing in the interval $[a, x_0]$ and monotonically decreasing in the interval $[x_0, b]$ when $a < x_0 < b$. Thus, we know that for $x$ in the interval $[a, x_0)$:

$$\frac{d|\psi_k(x)|^2}{dx} > 0. \tag{B4}$$

Equation (B4) implies $\text{sign}(v)\gamma_{\text{global}}(x) > 0$ for all $x$ in the interval $[a, x_0)$. Similarly, for $x$ in the interval $(x_0, b]$:

$$\frac{d|\psi_k(x)|^2}{dx} < 0. \tag{B5}$$

This constraint implies $\text{sign}(v)\gamma_{\text{global}}(x) < 0$ for all $x$ in the interval $(x_0, b]$. Combining these results, we conclude that a class-I global dissipation's domain wall must exist if the chiral mode with negative speed is localized.

Likewise, if a chiral mode with negative speed is localized at $x_0$, by following the same logic, we can conclude that a class-II global dissipation's domain wall must exist for a localized chiral mode with positive speed.

## APPENDIX C: NON-HERMITIAN CHIRAL SKIN EFFECT WITH A PAIR OF UNIFORM GLOBAL DISSIPATION'S DOMAIN WALLS

We consider a pair of global dissipation's domain walls that separate the regions with different strengths of dissipation in the left or right region. The uniform global dissipation's domain walls are set as $\gamma(0 < x < L_1) = \gamma_1$, $\gamma(L_1 < x < L) = \gamma_2$, respectively. Then we have

$$\bar{\gamma} = \frac{1}{L}\int_0^L \gamma(x)dx = \frac{\gamma_1 \cdot L_1 + \gamma_2 \cdot (L - L_1)}{L}. \tag{C1}$$

According to Eq. (A7), in the left region $x \in [0, L_1]$, we have

$$\psi^{(1)}(x) = \frac{1}{\mathcal{N}_1} e^{ikx} e^{\frac{1}{v}\int_0^x [\gamma(x)-\bar{\gamma}]dx} = \frac{1}{\mathcal{N}_1} e^{ikx} e^{\alpha_1 x}, \tag{C2}$$

where $\alpha_1 = \frac{(\gamma_1-\gamma_2)\cdot(L-L_1)}{vL}$. In the right region $x \in [L_1, L]$, we have

$$\begin{aligned}\psi^{(2)}(x) &= \frac{1}{\mathcal{N}_2} e^{ikx} e^{\frac{1}{v}\int_{L_1}^x [\gamma(x)-\bar{\gamma}]dx} \\ &= \frac{1}{\mathcal{N}_2} e^{ikx} e^{\alpha_2 (x-L)},\end{aligned} \tag{C3}$$

where $\alpha_2 = \frac{(\gamma_2-\gamma_1)\cdot L_1}{vL}$.Applying the boundary conditions $\psi^{(1)}(0) = \psi^{(2)}(L)$, $\psi^{(1)}(L_1) = \psi^{(2)}(L_1)$, we set $\mathcal{N}_1 = e^{\alpha_1 \cdot L_1}$, $\mathcal{N}_2 = 1$. Finally, we have

$$\begin{aligned}\psi^{(1)}(x) &= \frac{1}{e^{\alpha_1 \cdot L_1}} e^{ikx} e^{\frac{(\gamma_1-\gamma_2)\cdot(L-L_1)}{vL}x}, \\ \psi^{(2)}(x) &= e^{ikx} e^{\frac{(\gamma_2-\gamma_1)\cdot L_1}{vL}(x-L)}.\end{aligned} \tag{C4}$$

For the case 1 of $L_1 = L/2$, $\gamma(0 < x < L/2) = \gamma_1; \gamma(L/2 < x < L) = \gamma_2$, we have $\alpha_1 = \frac{\gamma_1-\gamma_2}{2v}$ and $\alpha_2 = \frac{\gamma_2-\gamma_1}{2v}$. The wave function of the edge states for a given wave number $k$ in the presence of the domain the wall is given by

$$\begin{aligned}\psi^{(1)}(x) &= \frac{1}{e^{\frac{(\gamma_1-\gamma_2)\cdot L}{4v}}} e^{ikx} e^{\frac{\gamma_1-\gamma_2}{2v}x}, \\ \psi^{(2)}(x) &= e^{ikx} e^{\frac{\gamma_2-\gamma_1}{2v}(x-L)},\end{aligned} \tag{C5}$$

where $\xi$ is the localization length, which is given by

$$\xi = \frac{2v}{|\gamma_2 - \gamma_1|}. \tag{C6}$$

The following is a discussion of the specific physical implications of this example.

*Example 1.* The effective model corresponds to Figs. 2(a) and 3(b) in the main text. The parameters are set as $L_1 = L/2$, $\gamma(0 < x < L/2) = -\gamma$ and $\gamma(L/2 < x < L) = \gamma$.

In this case, $\alpha_1 = -\frac{\gamma}{v}$ and $\alpha_2 = \frac{\gamma}{v}$ . The wave function of the edge states for a given wave number $k$ in the presence of the domain wall is given by

$$\begin{aligned}\psi^{(1)}(x) &= \frac{1}{e^{\frac{\gamma L}{2v}}} e^{ikx} e^{-\frac{\gamma}{v}x}, \\ \psi^{(2)}(x) &= e^{ikx} e^{\frac{\gamma}{v}(x-L)},\end{aligned} \tag{C7}$$

where $\xi$ is the localization length, which is given by

$$\xi = \frac{v}{\gamma}. \tag{C8}$$

*Example 2.* The effective model corresponds to Fig. 2(b) in the main text. The parameters are set as $\text{L}_1 = \text{L}/2$, $\gamma(0 < x < L/2) = -\gamma$, and $\gamma(L/2 < x < L) = 0$.

In this case, $\alpha_1 = -\frac{\gamma}{2v}$ and $\alpha_2 = \frac{\gamma}{2v}$. The wave function of the edge states for a given wave number $k$ in the presence of the domain wall is given by

$$\begin{aligned}\psi^{(1)}(x) &= \frac{1}{e^{\frac{\gamma L}{2v}}} e^{ikx} e^{-\frac{\gamma}{2v}x}, \\ \psi^{(2)}(x) &= e^{ikx} e^{\frac{\gamma}{2v}(x-L)},\end{aligned} \tag{C9}$$

where $\xi$ is the localization length, which is given by

$$\xi = \frac{2v}{\gamma}. \tag{C10}$$

## APPENDIX D: CALCULATE THE MOMENTUM CUTOFF IN THE HALDANE MODEL

We calculate the momentum cutoff in the Haldane model by using the transfer matrix approach.

For the Haldane model with zigzag edges, The standard transfer-matrix form can be written as

$$\begin{pmatrix}\varphi_n\\ \varphi_{n-1}\end{pmatrix}=\begin{pmatrix}t & -1\\ 1 & 0\end{pmatrix}\begin{pmatrix}\varphi_{n-1}\\ \varphi_{n-2}\end{pmatrix}=\widetilde{T}(\epsilon)\begin{pmatrix}\varphi_{n-1}\\ \varphi_{n-2}\end{pmatrix}, \tag{D1}$$

where $t=\frac{b+\sqrt{b^2+4(2+d)}}{2}$. If the Haldane model has an on-site term $M=0$ and the flux $\phi=\pi/2$, the parameter can be expressed as

$$b=\frac{1}{g_+g_-}\Big[2(g_++g_-)\epsilon+2g_0\Big(t_1-\frac{t_2^2}{t_1}\Big)+4t_2^2\cos\frac{3\sqrt{3}}{2}k_x\Big], \tag{D2}$$

$$d=\frac{1}{g_+g_-}\big[2\big(t_1^2-\epsilon^2\big)-f_+f_-\big]-2, \tag{D3}$$

$$f_\pm=2t_2\cos(\sqrt{3}k_x\pm\pi/2), \tag{D4}$$

$$g_\pm=2t_2\cos\left(\frac{\sqrt{3}}{2}k_x\pm\pi/2\right), \tag{D5}$$

$$g_0=72t_1\cos\frac{\sqrt{3}}{2}k_x. \tag{D6}$$

We set $\varphi_0$ and $\varphi_{L_y}$ as the wave function at the edge, then reduced the transfer matrix as follows

$$\begin{pmatrix}\varphi_{L_y+1}\\ \varphi_{L_y}\end{pmatrix}=T(\epsilon)\begin{pmatrix}\varphi_1\\ \varphi_0\end{pmatrix}, \tag{D7}$$

$$T(\epsilon)=[\widetilde{T}(\epsilon)]^{L_y}=\begin{pmatrix}T_{11}(\epsilon) & T_{12}(\epsilon)\\ T_{21}(\epsilon) & T_{22}(\epsilon)\end{pmatrix}. \tag{D8}$$

By using Furstenberg's theorem and the open boundary condition $\varphi_0=\varphi_{L_y+1}=0$, we can get the state localized at the edges satisfying $|T_{11}(\epsilon)|\ll 1$ localized at the lower edge (y=1), and $|T_{11}(\epsilon)|\gg 1$ localized at the upper edge ($y=L_y$). Note that this ansatz was already obtained in Ref. [76].

We consider the topological edge states localized at the lower edge ($y=1$) as an example, it satisfy $|T_{11}(\epsilon)|\ll 1$, which equivalent to $t(\epsilon)\ll 1$. We set $t_1=1$, $t_2=0.2$. According to Ref. [77], the $\epsilon(k)$ satisfy

$$\epsilon(k)=\frac{6t_1t_2}{\sqrt{t_1^2+8t_2^2(1-\cos k_x)}}\sin k_x. \tag{D9}$$

By using the above parameters, we get the numerical momentum cutoff. As shown in Fig. 12, the numerical momentum cutoff is about $k_x\in[-0.56\pi,0.56\pi]$, $k_0=0.56\pi$.

## APPENDIX E: NON-HERMITIAN CHIRAL SKIN EFFECT WITH MULTIPLE GLOBAL DISSIPATION'S DOMAIN WALLS

In this part, we consider multiple uniform global dissipation's domain walls that divide into $n$ regions based on different strengths of dissipation. System total length is $L$, with a dissipation of $\gamma_1$ over a length of $L_1$, a dissipation of $\gamma_2$ over a length of $L_2$, and a dissipation of $\gamma_n$ over a length of $L_n$. The uniform global dissipation's domain walls are set as $\gamma(0<x<L_1)=\gamma_1,\gamma(L_1<x<L_2+L_1)=\gamma_2,\ldots$, and

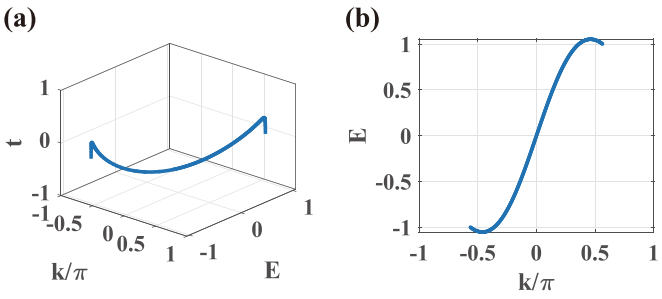


FIG. 12. The momentum cutoff in the Haldane model with $t_2=0.2t_1$.

$\gamma(L-L_n<x<L)=\gamma_n$, where $\Sigma_nL_n=L$. Then we have

$$\bar{\gamma}=\frac{1}{L}\int_0^L\gamma(x)dx=\frac{\gamma_1\cdot L_1+\gamma_2\cdot L_2+\gamma_3\cdot L_3+\cdots+\gamma_n\cdot L_n}{L}, \tag{E1}$$

where

$$\begin{aligned}\alpha_1&=-\frac{\gamma_1\cdot(L_1-L)+\gamma_2\cdot L_2+\gamma_3\cdot L_3+\cdots+\gamma_n\cdot L_n}{vL},\\ \alpha_2&=-\frac{\gamma_1\cdot L_1+\gamma_2\cdot(L_2-L)+\gamma_3\cdot L_3+\cdots+\gamma_n\cdot L_n}{vL},\\ \alpha_n&=-\frac{\gamma_1\cdot L_1+\gamma_2\cdot L_2+\gamma_3\cdot L_3+\cdots+\gamma_n\cdot(L_n-L)}{vL},\end{aligned} \tag{E2}$$

According to Eq. (A7), the wave function is given

$$\begin{aligned}\psi^{(1)}(x)&=\frac{1}{\mathcal{N}_1}e^{ikx}e^{\alpha_1x},\\ \psi^{(2)}(x)&=\frac{1}{\mathcal{N}_2}e^{ikx}e^{\alpha_2(x-L_1)},\\ \psi^{(n)}(x)&=\frac{1}{\mathcal{N}_n}e^{ikx}e^{\alpha_n(x-L_{n-1})}.\end{aligned} \tag{E3}$$

According to continuous condition, $\psi^{(1)}(0)=\psi^{(n)}(L)$, $\psi^{(1)}(L_1)=\psi^{(2)}(L_1)$, $\psi^{(2)}(L_2)=\psi^{(3)}(L_2)$, $\ldots,\psi^{(n-1)}(L_{n-1})=\psi^{(n)}(L_{n-1})$. Finally, we can get

$$\mathcal{N}_n=e^{-\Sigma_{i=n-1,i\in\mathbb{N}^+}[\alpha_i\cdot(L_i-L_{i-1})]}, \tag{E4}$$

where $\mathcal{N}_1=1$, and $L_0=0$.

The following is a discussion of the specific multiglobal dissipation's domain walls in Fig. 6(a). The parameters are set as $L_i=L/4$ $(i\in\{1,2,3,4\})$, $\gamma_1(0<x<L/4)=\gamma_{\text{eff}}^{\text{zigzag}}=-\gamma$, $\gamma_2(L/4<x<L/2)=\gamma_{\text{eff}}^{\text{armchair}}=0$, $\gamma_3(L/2<x<3L/4)=\gamma_{\text{eff}}^{\text{zigzag}}=\gamma$, and $\gamma_4(3L/4<x<L)=\gamma_{\text{eff}}^{\text{armchair}}=0$.

In this case, $\alpha_1=-\frac{3\gamma}{4v}$, $\alpha_3=\frac{3\gamma}{4v}$, and $\alpha_2=\alpha_4=0$. The wave function of the edge states for a given wave number $k$ in the presence of the domain wall is given by

$$\begin{aligned}\psi^{(1)}(x)&=e^{ikx}e^{-\frac{3\gamma}{4v}x},\\ \psi^{(2)}(x)&=\psi^{(4)}(x)=e^{ikx},\\ \psi^{(3)}(x)&=e^{-\frac{3\gamma L}{16v}}e^{ikx}e^{\frac{3\gamma}{4v}(x-L/2)},\end{aligned} \tag{E5}$$

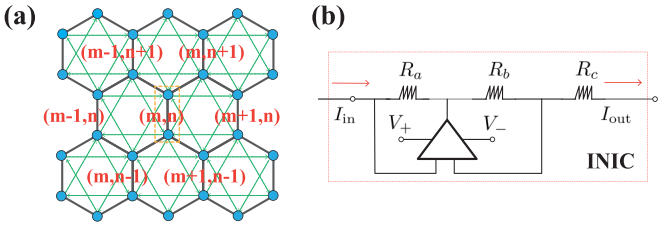


FIG. 13. (a) Schematic of the non-Hermitian Haldane model with uniform dissipation in bulk in the designed circuit. (b) The schematic diagram of an electrical circuit for realizing the negative resistance.

where $\xi$ is the localization length on zigzag edges, which is given by

$$\xi = \frac{4v}{3\gamma}. \tag{E6}$$

## APPENDIX F: THEORETICAL MODEL OF THE DESIGNED ELECTRIC CIRCUIT

In this part, we theoretically demonstrate the correspondence between the non-Hermitian Haldane model with uniform dissipation in bulk and our designed electric circuit, as show in Fig. 13. Based on Kirchhoff's law, the relationship between current and voltage at node $m$ is described by

$$I_m = \left[\sum_n iwC_{mn}(V_m - V_n) + \sum_n \frac{1}{iwL_{mn}}(V_m - V_n) + iwC_gV_m + \frac{V_m}{R_m}\right], \tag{F1}$$

where $I_m$ and $V_m$ are the net current and voltage of node $m$ with angular frequency being $\omega$. $L_{mn}$ is the inductance between node $m$ and node $n$. $C_{mn}$ is the capacitance between node $m$ and node $n$. The summation is taken over all nodes, which are connected to node $m$ through an inductor or a capacitor. $C_g$ is the grounding capacitor at node $m$. $R_m$ is the resistor or negative resistor at node $m$.

In PBC with loss in bulk, each lattice site possesses four nodes $(X^+, X^-, Y^+, Y^-)$. In this case, the voltage and current at the site $i$ should be written as: $V_i = [V_{i,X^+}, V_{i,X^-}, V_{i,Y^+}, V_{i,Y^-}]^T$ and $I_i = [I_{i,X^+}, I_{i,X^-}, I_{i,Y^+}, I_{i,Y^-}]^T$. Additionally, each site (grounded through $C_g$) is connected with other sites through two kinds of coupling: (three) nearest-neighbor couplings ($C_1$), (six) next-nearest-neighbor couplings ($C_2$). Also, the next-nearest-neighbor couplings are directional-dependent, and the coupling pattern determines the sign of the geometric phase $\varphi = \pi/2$.

In this case, the Kirchhoff equation on node $X^+(m, n, A)$ can be expressed as

$$\begin{aligned} I^A_{m,n,X^+} = &\left(i\omega C_g + \frac{1}{R_{g,A}}\right)V^A_{m,n,X^+} + \frac{1}{iwL}\left(V^A_{m,n,X^+} - V^A_{m,n,X^-}\right) \\ &+ iwC_1\left[\left(V^A_{m,n,X^+} - V^B_{m,n,X^+}\right) + \left(V^A_{m,n,X^+} - V^B_{m,n-1,X^+}\right) + \left(V^A_{m,n,X^+} - V^B_{m+1,n-1,X^+}\right)\right] \\ &+ iwC_2\left[\left(V^A_{m,n,X^+} - V^A_{m+1,n-1,Y^-}\right) + \left(V^A_{m,n,X^+} - V^A_{m,n-1,Y^+}\right) + \left(V^A_{m,n,X^+} - V^A_{m,n+1,Y^-}\right)\right. \\ &\left. + \left(V^A_{m,n,X^+} - V^A_{m+1,n,Y^+}\right) + \left(V^A_{m,n,X^+} - V^A_{m-1,n,Y^-}\right) + \left(V^A_{m,n,X^+} - V^A_{m-1,n+1,Y^+}\right)\right]. \end{aligned} \tag{F2}$$

The Kirchhoff equation on node $X^-$ can be expressed as

$$\begin{aligned} I^A_{m,n,X^-} = &\left(iwC_g + \frac{1}{R_{g,A}}\right)V^A_{m,n,X^-} + \frac{1}{iwL}\left(V^A_{m,n,X^-} - V^A_{m,n,X^+}\right) \\ &+ iwC_1\left[\left(V^A_{m,n,X^-} - V^B_{m,n,X^-}\right) + \left(V^A_{m,n,X^-} - V^B_{m,n-1,X^-}\right) + \left(V^A_{m,n,X^-} - V^B_{m+1,n-1,X^-}\right)\right] \\ &+ iwC_2\left[\left(V^A_{m,n,X^-} - V^A_{m+1,n-1,Y^+}\right) + \left(V^A_{m,n,X^-} - V^A_{m,n-1,Y^-}\right) + \left(V^A_{m,n,X^-} - V^A_{m,n+1,Y^+}\right)\right. \\ &\left. + \left(V^A_{m,n,X^-} - V^A_{m+1,n,Y^-}\right) + \left(V^A_{m,n,X^-} - V^A_{m-1,n,Y^+}\right) + \left(V^A_{m,n,X^-} - V^A_{m-1,n+1,Y^-}\right)\right]. \end{aligned} \tag{F3}$$

We assume that there are no external sources so that the current flows out of each node is zero ($I_i = [I_{i,X^+}, I_{i,X^-}, I_{i,Y^+}, I_{i,Y^-}]^T = 0$). In this case, Eqs. (F2) and (F3) become

$$\begin{aligned} 0 = &\left(iwC_g + \frac{1}{R_{g,A}} + 3iwC_1 + 6iwC_2\right)V^A_{m,n,X^+} + \frac{1}{iwL}\left(V^A_{m,n,X^+} - V^A_{m,n,X^-}\right) - iwC_1\left(V^B_{m,n,X^+} + V^B_{m,n-1,X^+} + V^B_{m+1,n-1,X^+}\right) \\ &- iwC_2\left(V^A_{m+1,n,Y^+} + V^A_{m-1,n,Y^-} + V^A_{m-1,n+1,Y^+} + V^A_{m+1,n-1,Y^-} + V^A_{m,n-1,Y^+} + V^A_{m,n+1,Y^-}\right) \end{aligned} \tag{F4}$$

and

$$\begin{aligned} 0 = &\left(iwC_g + \frac{1}{R_{g,A}} + 3iwC_1 + 6iwC_2\right)V^A_{m,n,X^-} + \frac{1}{iwL}\left(V^A_{m,n,X^-} - V^A_{m,n,X^+}\right) \\ &- iwC_1\left(V^B_{m,n,X^-} + V^B_{m,n-1,X^-} + V^B_{m+1,n-1,X^-}\right) \\ &- iwC_2\left(V^A_{m+1,n,Y^-} + V^A_{m-1,n,Y^+} + V^A_{m-1,n+1,Y^-} + V^A_{m+1,n-1,Y^+} + V^A_{m,n-1,Y^-} + V^A_{m,n+1,Y^+}\right). \end{aligned} \tag{F5}$$

For convenience, the capacitance is set as $C_g = C$, $C_1 = t_1 C$, and $C_2 = t_2 C$, where $C$ acts as a reference capacitance. And we set $M_{A(B)} = \frac{1}{iwCR_{g,A(B)}}$. Each pair of the LC circuit has the same resonance frequency $w_0 = 1/\sqrt{LC}$. We simply Eqs. (F4) and (F5) as

$$V^A_{m,n,X^+} - V^A_{m,n,X^-} = -\frac{w^2}{w_0^2}\big[-(M_A + 1 + 3t_1 + 6t_2)V^A_{m,n,X^+} + t_1\big(V^B_{m,n,X^+} + V^B_{m,n-1,X^+} + V^B_{m+1,n-1,X^+}\big) + t_2\big(V^A_{m+1,n,Y^+} + V^A_{m-1,n,Y^-} + V^A_{m-1,n+1,Y^+} + V^A_{m+1,n-1,Y^-} + V^A_{m,n-1,Y^+} + V^A_{m,n+1,Y^-}\big)\big] \tag{F6}$$

and

$$V^A_{m,n,X^-} - V^A_{m,n,X^+} = -\frac{w^2}{w_0^2}\big[-(M_A + 1 + 3t_1 + 6t_2)V^A_{m,n,X^-} + t_1\big(V^B_{m,n,X^-} + V^B_{m,n-1,X^-} + V^B_{m+1,n-1,X^-}\big) + t_2\big(V^A_{m+1,n,Y^-} + V^A_{m-1,n,Y^+} + V^A_{m-1,n+1,Y^-} + V^A_{m+1,n-1,Y^+} + V^A_{m,n-1,Y^-} + V^A_{m,n+1,Y^+}\big)\big]. \tag{F7}$$

The voltages across the inductors are set $U_X = V_{X^+} - V_{X^-}$, and $U_Y = V_{Y^+} - V_{Y^-}$. The difference between Eqs. (F6) and (F7) yields

$$U^A_{m,n,X} = -\frac{w^2}{2w_0^2}\big[-(M_A + 1 + 3t_1 + 6t_2)U^A_{m,n,X} + t_1\big(U^B_{m,n,X} + U^B_{m,n-1,X} + U^B_{m+1,n-1,X}\big) + t_2\big(U^A_{m+1,n,Y} - U^A_{m-1,n,Y} + U^A_{m-1,n+1,Y} - U^A_{m+1,n-1,Y} + U^A_{m,n-1,Y} - U^A_{m,n+1,Y}\big)\big]. \tag{F8}$$

We can also derive the equations for inductor $Y$ at site A, as well as for site B following the same route:

$$U^A_{m,n,Y} = -\frac{w^2}{2w_0^2}\big[-(M_A + 1 + 3t_1 + 6t_2)U^A_{m,n,Y} + t_1\big(U^B_{m,n,Y} + U^B_{m,n-1,Y} + U^B_{m+1,n-1,Y}\big) + t_2\big(-U^A_{m+1,n,X} + U^A_{m-1,n,X} - U^A_{m-1,n+1,X} + U^A_{m+1,n-1,X} - U^A_{m,n-1,X} + U^A_{m,n+1,X}\big)\big], \tag{F9}$$

$$U^B_{m,n,X} = -\frac{w^2}{2w_0^2}\big[-(M_B + 1 + 3t_1 + 6t_2)U^B_{m,n,X} + t_1\big(U^A_{m,n,X} + U^A_{m,n+1,X} + U^A_{m-1,n+1,X}\big) + t_2\big(-U^B_{m+1,n,Y} + U^B_{m-1,n,Y} - U^B_{m-1,n+1,Y} + U^B_{m+1,n-1,Y} - U^B_{m,n-1,Y} + U^B_{m,n+1,Y}\big)\big], \tag{F10}$$

$$U^B_{m,n,Y} = -\frac{w^2}{2w_0^2}\big[-(M_B + 1 + 3t_1 + 6t_2)U^B_{m,n,Y} + t_1\big(U^A_{m,n,Y} + U^A_{m,n+1,Y} + U^A_{m-1,n+1,Y}\big) + t_2\big(U^B_{m+1,n,X} - U^B_{m-1,n,X} + U^B_{m-1,n+1,X} - U^B_{m+1,n-1,X} + U^B_{m,n-1,X} - U^B_{m,n+1,X}\big)\big]. \tag{F11}$$

Defining $U_{\uparrow,\downarrow} = U_X \pm iU_Y$, we obtain

$$\left(3t_1 + 6t_2 + 1 - \frac{2w_0^2}{w^2}\right)U^A_{m,n,\uparrow} = -M_A U^A_{m,n,\uparrow} + t_1\big(U^B_{m,n,\uparrow} + U^B_{m,n-1,\uparrow} + U^B_{m+1,n-1,\uparrow}\big) + t_2\big(e^{-i\varphi}U^A_{m+1,n,\uparrow} + e^{i\varphi}U^A_{m-1,n,\uparrow} + e^{-i\varphi}U^A_{m-1,n+1,\uparrow} + e^{i\varphi}U^A_{m+1,n-1,\uparrow} + e^{-i\varphi}U^A_{m,n-1,\uparrow} + e^{i\varphi}U^A_{m,n+1,\uparrow}\big) \tag{F12}$$

and

$$\left(3t_1 + 6t_2 + 1 - \frac{2w_0^2}{w^2}\right)U^B_{m,n,\uparrow} = -M_B U^B_{m,n,\uparrow} + t_1\big(U^A_{m,n,\uparrow} + U^A_{m,n+1,\uparrow} + U^A_{m-1,n+1,\uparrow}\big) + t_2\big(e^{i\varphi}U^B_{m+1,n,\uparrow} + e^{-i\varphi}U^B_{m-1,n,\uparrow} + e^{i\varphi}U^B_{m-1,n+1,\uparrow} + e^{-i\varphi}U^B_{m+1,n-1,\uparrow} + e^{i\varphi}U^B_{m,n-1,\uparrow} + e^{-i\varphi}U^B_{m,n+1,\uparrow}\big), \tag{F13}$$

where the geometric phase $\varphi = \pi/2$.

Consider nearest-neighbor coupling $U^B_{m,n} = e^{i\mathbf{k}\mathbf{e}_1}U^A_{m,n}$, $U^B_{m+1,n-1} = e^{i\mathbf{k}\mathbf{e}_2}U^A_{m,n}$, $U^B_{m,n-1} = e^{i\mathbf{k}\mathbf{e}_3}U^A_{m,n}$, and next-nearest-neighbor coupling $U^A_{m-1,n} = e^{i\mathbf{k}\mathbf{v}_1}U^A_{m,n}$, $U^A_{m,n+1} = e^{i\mathbf{k}\mathbf{v}_2}U^A_{m,n}$, $U^A_{m+1,n-1} = e^{i\mathbf{k}\mathbf{v}_3}U^A_{m,n}$, we can get the independent equation for $U_\uparrow$ as

$$E\begin{bmatrix}U^A_{\mathbf{k},\uparrow}\\ U^B_{\mathbf{k},\uparrow}\end{bmatrix} = \begin{bmatrix}p_k(\varphi) - M_A & T_\mathbf{k}\\ T^*_\mathbf{k} & p_k(-\varphi) - M_B\end{bmatrix}\begin{bmatrix}U^A_{\mathbf{k},\uparrow}\\ U^B_{\mathbf{k},\uparrow}\end{bmatrix}, \tag{F14}$$

where $E = 3t_1 + 6t_2 + 1 - \frac{2w_0^2}{w^2}$, $p_k(\varphi) = 2t_2[\cos(\mathbf{k}\cdot\mathbf{v_1} + \varphi) + \cos(\mathbf{k}\cdot\mathbf{v_2} + \varphi) + \cos(\mathbf{k}\cdot\mathbf{v_3} + \varphi)]$, $T_\mathbf{k} = t_1(e^{i\mathbf{k}\mathbf{e}_1} + e^{i\mathbf{k}\mathbf{e}_2} + e^{i\mathbf{k}\mathbf{e}_3})$, and $M_{A(B)} = -\frac{i}{wCR_{g,A(B)}}$.

As a result, in eigenfrequency $\omega_0 = 1/\sqrt{LC}$, the corresponding dissipation is $i\gamma_{A(B)} = -M_{A(B)} = \frac{i}{R_{g,A(B)}}\sqrt{\frac{L}{C}}$. It's to be noted that $R_{g,A(B)}$ can be negative by using INIC, which corresponded to gain in the non-Hermitian Haldane model.

Equations (9) and (F14) share the same noninteracting Hamiltonian and nearly all physical quantities are defined based on the Hamiltonian should be the same. The corresponding eigenvalue is $E$, and the eigenstate is $[U^A_{\mathbf{k},\uparrow}, U^B_{\mathbf{k},\uparrow}]^T$, which can be regarded as the wave function of the Haldane model with dissipation. Based on the consistency of the mathematical formula, it is straightforward to infer that we can implement the Haldane model by using designed electric circuits in Fig. 13.

To realize a non-Hermitian Haldane model with uniform dissipation in bulk, the schematic of the designed electric circuit is shown in Fig. 13(a). Electric circuits include circuit components such as capacitors, inductors, resistors, and negative impedance converters with current inversion (INIC). As shown in Fig. 13(b), INIC can cause the current to flow in the opposite direction to the voltage, so it can be regarded as a negative resistor [74].


[1] H. Shen, B. Zhen, and L. Fu, Topological band theory for non-Hermitian Hamiltonians, Phys. Rev. Lett. **120**, 146402 (2018).

[2] T. Liu, Y. R. Zhang, Q. Ai, Z. Gong, K. Kawabata, M. Ueda, and F. Nori, Second-order topological phases in non-Hermitian systems, Phys. Rev. Lett. **122**, 076801 (2019).

[3] X. W. Luo and C. Zhang, Higher-order topological corner states induced by gain and loss, Phys. Rev. Lett. **123**, 073601 (2019).

[4] N. Matsumoto, K. Kawabata, Y. Ashida, S. Furukawa, and M. Ueda, Continuous phase transition without gap closing in non-Hermitian quantum many-body systems, Phys. Rev. Lett. **125**, 260601 (2020).

[5] F. Yang, H. Wang, M. L. Yang, C. X. Guo, X. R. Wang, G. Y. Sun, and S. P. Kou, Hidden continuous quantum phase transition without gap closing in non-Hermitian transverse ising model, New J. Phys. **24**, 043046 (2022).

[6] Y. Ashida, Z. Gong, and M. Ueda, Non-Hermitian physics, Adv. Phys. **69**, 249 (2020).

[7] C. X. Guo, X. R. Wang, C. Wang, and S. P. Kou, Non-Hermitian dynamic strings and anomalous topological degeneracy on a non-Hermitian toric-code model with parity-time symmetry, Phys. Rev. B **101**, 144439 (2020).

[8] W. Wang and Z. Ma, Concurrence of anomalous hall effect and charge density wave in a superconducting topological kagome metal, Phys. Rev. B **106**, 115306 (2022).

[9] C. M. Bender and S. Boettcher, Real spectra in non-Hermitian Hamiltonians having $\mathscr{PT}$ symmetry, Phys. Rev. Lett. **80**, 5243 (1998).

[10] E. J. Bergholtz, J. C. Budich, and F. K. Kunst, Exceptional topology of non-Hermitian systems, Rev. Mod. Phys. **93**, 015005 (2021).

[11] W. D. Heiss, The physics of exceptional points, J. Phys. A: Math. Theor. **45**, 444016 (2012).

[12] A. Guo, G. J. Salamo, D. Duchesne, R. Morandotti, M. Volatier-Ravat, V. Aimez, G. A. Siviloglou, and D. N. Christodoulides, Observation of $\mathcal{PT}$-symmetry breaking in complex optical potentials, Phys. Rev. Lett. **103**, 093902 (2009).

[13] L. Feng, Y.-L. Xu, W. S. Fegadolli, M.-H. Lu, J. E. Oliveira, V. R. Almeida, Y.-F. Chen, and A. Scherer, Experimental demonstration of a unidirectional reflectionless parity-time metamaterial at optical frequencies, Nat. Mater. **12**, 108 (2013).

[14] T. E. Lee, Anomalous edge state in a non-Hermitian lattice, Phys. Rev. Lett. **116**, 133903 (2016).

[15] Y. Xiong, Why does bulk boundary correspondence fail in some non-Hermitian topological models, J. Phys. Commun. **2**, 035043 (2018).

[16] V. M. Martinez Alvarez, J. E. Barrios Vargas, and L. E. F. Foa Torres, Non-Hermitian robust edge states in one dimension: anomalous localization and eigenspace condensation at exceptional points, Phys. Rev. B **97**, 121401(R) (2018).

[17] A. Ghatak and T. Das, New topological invariants in non-Hermitian systems, J. Phys.: Condens. Matter **31**, 263001 (2019).

[18] S. Yao and Z. Wang, Edge states and topological invariants of non-Hermitian systems, Phys. Rev. Lett. **121**, 086803 (2018).

[19] C. H. Lee and R. Thomale, Anatomy of skin modes and topology in non-Hermitian systems, Phys. Rev. B **99**, 201103(R) (2019).

[20] K. Yokomizo and S. Murakami, Non-Bloch band theory of non-Hermitian systems, Phys. Rev. Lett. **123**, 066404 (2019).

[21] C. X. Guo, C. H. Liu, X. M. Zhao, Y. Liu, and S. Chen, Exact solution of non-Hermitian systems with generalized boundary conditions: Size-dependent boundary effect and fragility of the skin effect, Phys. Rev. Lett. **127**, 116801 (2021).

[22] F. K. Kunst, E. Edvardsson, J. C. Budich, and E. J. Bergholtz, Biorthogonal bulk-boundary correspondence in non-Hermitian systems, Phys. Rev. Lett. **121**, 026808 (2018).

[23] C. Yin, H. Jiang, L. Li, R. Lü, and S. Chen, Geometrical meaning of winding number and its characterization of topological phases in one-dimensional chiral non-Hermitian systems, Phys. Rev. A **97**, 052115 (2018).

[24] F. Song, S. Yao, and Z. Wang, Non-Hermitian skin effect and chiral damping in open quantum systems, Phys. Rev. Lett. **123**, 170401 (2019).

[25] S. Longhi, Probing non-Hermitian skin effect and non-Bloch phase transitions, Phys. Rev. Res. **1**, 023013 (2019).

[26] D. S. Borgnia, A. J. Kruchkov, and R. J. Slager, Non-Hermitian boundary modes and topology, Phys. Rev. Lett. **124**, 056802 (2020).

[27] Y. Yi and Z. Yang, Non-Hermitian skin modes induced by on-site dissipations and chiral tunneling effect, Phys. Rev. Lett. **125**, 186802 (2020).

[28] N. Okuma and M. Sato, Non-Hermitian skin effects in hermitian correlated or disordered systems: Quantities sensitive or insensitive to boundary effects and pseudo-quantum-number, Phys. Rev. Lett. **126**, 176601 (2021).

[29] F. Roccati, Non-Hermitian skin effect as an impurity problem, Phys. Rev. A **104**, 022215 (2021).

[30] H. Zhang, T. Chen, L. Li, C. H. Lee, and X. Zhang, Electrical circuit realization of topological switching for the non-Hermitian skin effect, Phys. Rev. B **107**, 085426 (2023).

[31] R. Lin, Tommy Tai, L. Li and C. H. Lee, Topological non-Hermitian skin effect, Front. Phys. **18**, 53605 (2023).

[32] K. Yokomizo and S. Murakami, Non-Bloch bands in two-dimensional non-Hermitian systems, Phys. Rev. B **107**, 195112 (2023).

[33] Z. Ou, Y. Wang, and L. Li, Non-Hermitian boundary spectral winding, Phys. Rev. B **107**, L161404 (2023).

[34] Z. Zhang, M. Rosendo López, Y. Cheng, X. Liu, and J. Christensen, Non-Hermitian sonic second-order topological insulator, Phys. Rev. Lett. **122**, 195501 (2019).

[35] E. Edvardsson, F. K. Kunst, and E. J. Bergholtz, Non-Hermitian extensions of higher-order topological phases and their biorthogonal bulk-boundary correspondence, Phys. Rev. B **99**, 081302(R) (2019).

[36] K. Kawabata, M. Sato, and K. Shiozaki, Higher-order non-Hermitian skin effect, Phys. Rev. B **102**, 205118 (2020).

[37] X. Zhang, Y. Tian, J.-H. Jiang, M.-H. Lu, and Y.-F. Chen, Observation of higher-order non-Hermitian skin effect, Nat. Commun. **12**, 5377 (2021).

[38] L. Li, C. H. Lee, and J. Gong, Topological switch for non-Hermitian skin effect in cold-atom systems with loss, Phys. Rev. Lett. **124**, 250402 (2020).

[39] K. Zhang, Z. Yang, and C. Fang, Correspondence between winding numbers and skin modes in non-Hermitian systems, Phys. Rev. Lett. **125**, 126402 (2020).

[40] N. Okuma, K. Kawabata, K. Shiozaki, and M. Sato, Topological origin of non-Hermitian skin effects, Phys. Rev. Lett. **124**, 086801 (2020).

[41] Z. Yang, K. Zhang, C. Fang, and J. Hu, Non-Hermitian bulk-boundary correspondence and auxiliary generalized brillouin zone theory, Phys. Rev. Lett. **125**, 226402 (2020).

[42] T. S. Deng and W. Yi, Non-Bloch topological invariants in a non-Hermitian domain wall system, Phys. Rev. B **100**, 035102 (2019).

[43] L. Xiao, T. Deng, K. Wang, G. Zhu, Z. Wang, W. Yi, and P. Xue, Non-Hermitian bulk–boundary correspondence in quantum dynamics, Nat. Phys. **16**, 761 (2020).

[44] T. Helbig, T. Hofmann, S. Imhof, M. Abdelghany, T. Kiessling, L. W. Molenkamp, C. H. Lee, A. Szameit, M. Greiter, and R. Thomale, Generalized bulk–boundary correspondence in non-Hermitian topolectrical circuits, Nat. Phys. **16**, 747 (2020).

[45] T. Hofmann, T. Helbig, F. Schindler, N. Salgo, M. Brzezińska, M. Greiter, T. Kiessling, D. Wolf, A. Vollhardt, A. Kabaši, C. H. Lee, A. Bilušić, R. Thomale, and T. Neupert, Reciprocal skin effect and its realization in a topolectrical circuit, Phys. Rev. Res. **2**, 023265 (2020).

[46] L. Herviou, J. H. Bardarson, and N. Regnault, Defining a bulk-edge correspondence for non-Hermitian Hamiltonians via singular-value decomposition, Phys. Rev. A **99**, 052118 (2019).

[47] X. R. Wang, C. X. Guo, and S. P. Kou, Defective edge states and number-anomalous bulk-boundary correspondence in non-Hermitian topological systems, Phys. Rev. B **101**, 121116(R) (2020).

[48] X. R. Wang, C. X. Guo, Q. Du, and S. P. Kou, State-dependent topological invariants and anomalous bulk-boundary correspondence in non-Hermitian topological systems with generalized inversion symmetry, Chin. Phys. Lett. **37**, 117303 (2020).

[49] S. Mandal, R. Banerjee, E. A. Ostrovskaya, and T. C. H. Liew, Nonreciprocal transport of exciton polaritons in a non-Hermitian chain, Phys. Rev. Lett. **125**, 123902 (2020).

[50] S. Yao, F. Song, and Z. Wang, Non-Hermitian chern bands, Phys. Rev. Lett. **121**, 136802 (2018).

[51] K. Kawabata, K. Shiozaki, and M. Ueda, Anomalous helical edge states in a non-Hermitian chern insulator, Phys. Rev. B **98**, 165148 (2018).

[52] Y. Chen and H. Zhai, Hall conductance of a non-Hermitian Chern insulator, Phys. Rev. B **98**, 245130 (2018).

[53] M. R. Hirsbrunner, T. M. Philip, and M. J. Gilbert, Topology and observables of the non-Hermitian Chern insulator, Phys. Rev. B **100**, 081104(R) (2019).

[54] H. C. Wu, L. Jin, and Z. Song, Inversion symmetric non-Hermitian Chern insulator, Phys. Rev. B **100**, 155117 (2019).

[55] Y. Xiao and C. T. Chan, Topology in non-Hermitian Chern insulators with skin effect, Phys. Rev. B **105**, 075128 (2022).

[56] X. Q. Sun, P. Zhu, and T. L. Hughes, Geometric response and disclination-induced skin effects in non-Hermitian systems, Phys. Rev. Lett. **127**, 066401 (2021).

[57] F. Schindler and A. Prem, Dislocation non-Hermitian skin effect, Phys. Rev. B **104**, L161106 (2021).

[58] B. A. Bhargava, I. C. Fulga, J. Van Den Brink, and A. G. Moghaddam, Non-Hermitian skin effect of dislocations and its topological origin, Phys. Rev. B **104**, L241402 (2021).

[59] F. Song, H. Y. Wang, and Z. Wang, Non-Bloch PT symmetry breaking: Universal threshold and dimensional surprise, *A Festschrift in Honor of the C N Yang Centenary* (2022), pp. 299–311.

[60] K. Zhang, Z. Yang, and C. Fang, Universal non-Hermitian skin effect in two and higher dimensions, Nat. Commun. **13**, 2496 (2022).

[61] C. H. Lee, L. Li, and J. Gong, Hybrid higher-order skin topological modes in non-reciprocal systems, Phys. Rev. Lett. **123**, 016805 (2019).

[62] D. Zou, T. Chen, W. He, J. Bao, C. H. Lee, H. Sun, and X. Zhang, Observation of hybrid higher-order skin-topological effect in non-Hermitian topolectrical circuits, Nat. Commun. **12**, 7201 (2021).

[63] Y. Li, C. Liang, C. Wang, C. Lu, and Y. C. Liu, Gain-loss-induced hybrid skin-topological effect, Phys. Rev. Lett. **128**, 223903 (2022).

[64] W. Zhu and J. Gong, Hybrid skin-topological modes without asymmetric couplings, Phys. Rev. B **106**, 035425 (2022).

[65] D. Wu, J. Chen, W. Su, R. Wang, B. Wang, and D. Y. Xing, Effective impurity behavior emergent from non-Hermitian proximity effect, Commun. Phys. **6**, 160 (2023).

[66] S. Mandal, R. Banerjee, and T. C. H. Liew, From the topological spin-hall effect to the non-Hermitian skin effect in an elliptical micropillar chain, ACS Photon. **9**, 527 (2022).

[67] W. Zhu and J. Gong, Photonic corner skin modes in non-Hermitian photonic crystals, Phys. Rev. B **108**, 035406 (2023).

[68] F. Schindler, K. Gu, B. Lian, and K. Kawabata, Hermitian bulk–non-Hermitian boundary correspondence, PRX Quantum **4**, 030315 (2023).

[69] G. G. Liu, S. Mandal, P. Zhou, X. Xi, R. Banerjee, Y. H. Hu, M. Wei, M. Wang, Q. Wang, Z. Gao, H. Chen, Y. Yang, Y. Chong, and B. Zhang, Localization of chiral edge states by the non-Hermitian skin effect, arXiv:2305.13139.

[70] F. D. M. Haldane, Model for a quantum hall effect without landau levels: Condensed-matter realization of the "Parity Anomaly", Phys. Rev. Lett. **61**, 2015 (1988).

[71] G. Jotzu, M. Messer, R. Desbuquois, M. Lebrat, T. Uehlinger, D. Greif, and T. Esslinger, Experimental realization of the topological Haldane model with ultracold fermions, Nature (London) **515**, 237 (2014).

[72] J. Zhang, Z.-Q. Zhang, S.-G. Cheng, and H. Jiang, Topological Anderson insulator via disorder-recovered average symmetry, Phys. Rev. B **106**, 195304 (2022).

[73] Y. Yang, D. Zhu, Z. Hang, and Y. Chong, Observation of antichiral edge states in a circuit lattice, Sci. China: Phys., Mech. Astron. **64**, 257011 (2021).

[74] S. Liu, S. Ma, C. Yang, L. Zhang, W. Gao, J. Yuan, J. Tie, and S. Zhang, Gain- and loss-induced topological insulating phase in a non-Hermitian electrical circuit, Phys. Rev. Appl. **13**, 014047 (2020).

[75] D. Nakamura, K. Inaka, N. Okuma, and M. Sato, Universal platform of point-gap topological phases from topological materials, Phys. Rev. Lett. **131**, 256602 (2023).

[76] N. Hao, P. Zhang, Z. Wang, W. Zhang, and Y. Wang, Topological edge states and quantum hall effect in the Haldane model, Phys. Rev. B **78**, 075438 (2008).

[77] Z. Huang and D. P. Arovas, Edge states, Entanglement spectra, and wannier functions in Haldane's honeycomb lattice model and its bilayer generalization, arXiv:1205.6266.